

# Brain Targeting of Citicoline Sodium via Hyaluronic Acid-Decorated Novel Nano-Transbilosomes for Mitigation of Alzheimer's Disease in a Rat Model: Formulation, Optimization, in vitro and in vivo Assessment

Kariman M AbouElhassan<sup>1,2</sup>, Hatem A Sarhan<sup>1</sup>, Amal K Hussein<sup>1</sup>, Ashraf Taye<sup>3</sup>, Yasmin M Ahmed<sup>4</sup>, Mohamed A Safwat<sup>5</sup>

<sup>1</sup>Department of Pharmaceutics, Faculty of Pharmacy, Minia University, Minia, 61519, Egypt; <sup>2</sup>Faculty of Pharmacy, South Valley University, Qena, 83523, Egypt; <sup>3</sup>Department of Pharmacology and Toxicology, Faculty of Pharmacy, South Valley University, Qena, 83523, Egypt; <sup>4</sup>Department of Pharmacology and Toxicology, Faculty of Pharmacy, Nahda University, Beni-Suef, 62514, Egypt; <sup>5</sup>Department of Pharmaceutics, Faculty of Pharmacy, South Valley University, Qena, 83523, Egypt

Correspondence: Kariman M AbouElhassan, Faculty of Pharmacy, South Valley University, El-Moatakal Street, Qena, Egypt, Tel +20 1008052043, Fax +20 963211279, Email karimanmusalim@yahoo.com

**Background:** Alzheimer's disease (AD) is one of the furthestmost advanced neurodegenerative disorders resulting in cognitive and behavioral impairment. Citicoline sodium (CIT) boosts the brain's secretion of acetylcholine, which aids in membrane regeneration and repair. However, it suffers from poor blood-brain barrier (BBB) permeation, which results in lower levels of CIT in the brain.

**Purpose:** This study targeted to encapsulate CIT into novel nano-platform transbilosomes decorated with hyaluronic acid CIT-HA\*TBLs to achieve enhanced drug delivery from the nose to the brain.

**Methods:** A method of thin-film hydration was utilized to prepare different formulae of CIT-TBLs using the Box-Behnken design. The optimized formula was then hyaluronated via integration of HA to form the CIT-HA\*TBLs formula. Furthermore, AD induction was performed by aluminum chloride (AlCl<sub>3</sub>), animals were allocated, and brain hippocampus tissue was isolated for ELISA and qRT-PCR analysis of malondialdehyde (MDA), nuclear factor kappa B (NF-kB), and microRNA-137 (miR-137) coupled with immunohistochemical amyloid-beta (Aβ<sub>1-42</sub>) expression and histopathological finding.

**Results:** The hyaluronated CIT-HA\*TBLs formula, which contained the following ingredients: PL (300 mg), Sp 60 (43.97 mg), and SDC (20 mg). They produced spherical droplets at the nanoscale (178.94 ± 12.4 nm), had a high entrapment efficiency with 74.92 ± 5.54%, had a sustained release profile of CIT with 81.27 ± 3.8% release, and had ex vivo permeation of CIT with 512.43 ± 19.58 μg/cm<sup>2</sup>. In vivo tests showed that CIT-HA\*TBL thermogel dramatically reduces the hippocampus expression of miR-137 and (Aβ<sub>1-42</sub>) expression, boosting cholinergic neurotransmission and decreasing MDA and NF-kB production. Furthermore, CIT-HA\*TBLs thermogel mitigate histopathological damage in compared to the other groups.

**Conclusion:** Succinctly, the innovative loading of CIT-HA\*TBLs thermogel is a prospectively invaluable intranasal drug delivery system that can raise the efficacy of CIT in Alzheimer's management.

**Keywords:** Alzheimer's disease, transbilosomes, Box-Behnken design, intranasal drug delivery, brain targeting, in vivo study

## Introduction

Alzheimer's disease (AD) is one of the furthestmost advanced neurodegenerative disorders in persons beyond 65 years of age producing loss of neurons and finally dementia.<sup>1</sup> It is caused due to neurodevelopmental disorders that result from an imbalance between excitatory and inhibitory signaling of the hippocampus and the cerebral cortex.<sup>2</sup> The extracellular precipitation of amyloid-beta (Aβ<sub>1-42</sub>) and the neurofibrillary tangles of hyper-phosphorylated tau proteins are intellect to

be the two vital pathologic hallmarks of AD,<sup>3</sup> associated with stimulating acetylcholine esterase (AChE) enzyme to form insoluble A $\beta$  plaques, induced neural cell death.<sup>4,5</sup> Consequently, these pathological neural structure changes result in memory loss and cognitive dysfunction in AD patients.<sup>6</sup>

However, the extracellular matrix (ECM) is a crucial key regulator for synapse formation and regulation of its function in the cerebral cortex.<sup>7</sup> When damage or alteration of the matrix arrangement occurs, it implicitly modulates neuronal activity, synaptic plasticity, and amyloid beta-42-A aggregation in AD.<sup>8</sup> Hyaluronic acid (HA) is a crucial component of the central nervous system and a scaffold component of the extracellular matrix (CNS).<sup>9</sup> It also modulates intercellular signaling through interactions with Hyaluronan neuronal cell surface receptors like Cluster of Differentiation 44 (CD44), Hyaluronan-mediated motility (RHAMM), and Intercellular adhesion molecule 1 (ICAM).<sup>10</sup> The degradation of hyaluronic acid as a result of an excessive inflammatory response brought on by tissue trauma and neurodegenerative disease leads to the remodeling of ECM of the nervous system.<sup>11</sup> The NF- $\kappa$ B pathway can be regulated by miRNA-137, which inhibits pro-inflammatory responses by targeting ICAM-1 and CD44, and tumor necrosis factor-alpha-Induced Protein 1 (TNFAIP1), inhibiting the neurodegenerative disorders of AD. The NF- $\kappa$ B pathway is also inhibited when miRNA-137 is overexpressed in neurons.<sup>12</sup>

Otherwise, the main cogitation centre was the central cholinergic system.<sup>13</sup> Acetylcholine (ACh) is the primary cholinergic neurotransmitter synthesis in the central neurons responsible for maintaining consciousness, recognition, thinking, and learning, especially in the basal forebrain, frontal lobe, hippocampus, and brainstem.<sup>14,15</sup> Decreased ACh levels in the brain significantly characterize AD; neurodegenerative dysfunction symptoms appear.<sup>15</sup>

Citicoline sodium (CIT) is a choline supplier, which is a substantial intermediate in the synthesis of phosphatidylcholine (indispensable brain phospholipids).<sup>16</sup> The neuroprotective drug CIT is therapeutically used to treat conditions such as Alzheimer's disease (AD), Parkinson's disease, stroke, and brain ischemia.<sup>16</sup> Citicoline can benefit both degenerative and vascular cognitive decline in an assortment of ways including (apoptosis suppression, neuroplasticity reinforcement, phospholipid, and acetylcholine ACh synthesis).<sup>17</sup> However, when CIT was taken orally or parenterally, it quickly converts to cytidine and choline in a few minutes.<sup>18</sup> These two separate metabolites are consumed by various parts of the body and then reach the brain. Even though the absorption of the drug is very high with a bioavailability of over 90%, the percentage drug delivered to the brain is very low, only 0.5% and 2% when taken orally or injected, respectively.<sup>19</sup> This may be clarified by the strong polarity of CIT and its fast metabolism followed by liver uptake of most of the free choline which represents the fundamental obstacle hindering intact drug molecules from crossing the blood-brain barrier.<sup>20</sup> These demands necessitate the development of an appropriate delivery nanocarrier to target the CIT directly to the brain and realize its therapeutic profit in AD.

One of the nanocarriers for the transport of active compounds that is now being explored the most frequently is the liposome. They are vesicular structures with a spherical form that range in size from 25 nm to a few microns and are made of phospholipids with a hydrophilic head and two hydrophobic tails.<sup>21,22</sup> There are many benefits of using liposomes as a drug delivery vehicle, including higher efficacy and bioavailability of encapsulated substances, high biodegradability and biocompatibility with low toxicity, ability to self-assemble, the encapsulation of both hydrophobic and hydrophilic agents, and possibility of facile removal from the body.<sup>23,24</sup> Additionally, these vesicular nanostructures enable the modification of important physicochemical characteristics, such as size and surface. The ability to change important physicochemical characteristics, such as size and surface, is another feature of these vesicular nanostructures that is essential in the application.<sup>25</sup> Liposomes have been utilized in the food, cosmetic, agricultural, and, most significantly, pharmaceutical industries since the 1960s.<sup>26</sup> As indicated by the fact that liposomes were the first nanoscopic drug delivery technology to be approved for clinical use (Doxil<sup>®</sup>, in 1995),<sup>27</sup> the development of this type of nanocarrier is really very dynamic and prospective.

Liposomes' insufficient chemical (hydrolysis of ester linkages or peroxidation of the unsaturated acyl chain) and physical (destabilisation processes such as agglomeration, flocculation, or coalescence, which ultimately lead to changes in the size of the nanostructure) stability limit their application.<sup>28</sup> Novel structural liposomes were created using supportive additives like cholesterol, ethanol, or non-ionic surfactants to improve the stability and efficacy of drug loading in conventional vesicle vehicles.

The second class of liposomes made of phospholipids and additional single-chain surfactants, also known as edge activators, are called transferosomes.<sup>29</sup> The use of transferosomes as a drug delivery vehicle has a variety of advantages, including its capacity to accommodate therapeutic molecules with a variety of solubilities due to their infrastructure, which combines hydrophobic and hydrophilic moieties. They can swell and squeeze through a tiny hole (between 5 and 10 times smaller than their own diameter) without suffering a substantial loss. Drugs of both low and high molecular weights, such as analgesics, anaesthetics, corticosteroids, sex hormone, anticancer, insulin, and albumin, can be transported via them. Protein and peptides are two examples of how they protect the medicine from metabolic deterioration. They serve as depots and release their contents gradually.<sup>30,31</sup> They can be utilized for both systemic and topical medication delivery. Because the technique is uncomplicated and avoids needless use of pharmaceutically undesirable ingredients, they are simple to scale up. That on first look, transferosomes resemble liposomes, a type of lipid bilayered vesicle. However, in terms of functionality, transferosomes are significantly more malleable and flexible than routinely employed liposomes. The fundamental drawback of transferosomes is that they are prone to oxidative destruction, which makes them chemically unstable.<sup>30</sup>

The most recent literature studies describe bilosomes, the next generation of “soft” lipid vesicular nanocarriers, in which bile salts such as deoxycholic acid, sodium cholate, or sorbitan tristearate operate as edge activators. Comparing the system to the traditional liposome and transferosomes, the addition of these biosurfactants boosts the colloidal stability of the system.<sup>32</sup> Bilosomes (BLs), which are mostly made of nonionic surfactants and bile salts, are a new approach to vesicular drug delivery.<sup>33,34</sup> They are metastable in membrane organization due to the incorporation of bile salt molecules that decrease the phase transition temperature producing them ultra-flexible and highly deformable under the physiological temperature.<sup>35</sup> Bilosomes have been applied for transdermal,<sup>36</sup> topical,<sup>37</sup> and ocular drug delivery.<sup>34</sup>

However, no more published studies have examined the impact of intranasal administration of medication-loaded BLs on absorption of drug and brain targeting. Although BL vesicles have not been considerably discussed for intranasal medicine delivery, their unique small size, incorporated with the bile salts in their constitution, supplies promising scenarios for using them in nose-to-brain drug delivery.

The theory of brain drug targeting using nose dosage form in the cure of neurodegenerative disorders has profited a great deal from nanoscience, provided that nanovesicles are capable of overcoming the fast mucociliary clearance and poor nasal absorption.<sup>38</sup> Intranasal delivery of nanovesicles offers various advantages, such as ease of self-administration, non-invasiveness as well as successful brain targeting.<sup>39</sup> Despite the multiple advantages of bilosomal vesicles, BL suitability as a systemic delivery vehicle is compromised owing to a lack of specificity and easy sequestration by the reticuloendothelial system.<sup>40</sup>

To get over these restrictions, these unique vesicles were created and fabricated by combining Span 60, Phospholipon 90 G, sodium deoxycholate, and cholesterol in various ratios to boost the rate of drug loading and enhance the vesicle’s ability to penetrate biological membranes; the resulting vesicle was given the name Transbilosome.

Ultra-flexible transbilosomes (TBLs) are an unique permeation-enhancing lipid nanovesicular system derived from bilosomes, which were initially defined by Conacher et al,<sup>41</sup> and from transferosomes, which Cevc and Blume established in 1992.<sup>29</sup> TBLs are elastic, malleable lipid vesicles that contain a variety of ratios of phospholipids, Span 60, cholesterol, and sodium deoxycholate. They effectively penetrate biological membranes, particularly nasal mucosa, due to their tiny particle size, high entrapment efficiency percentage, high in vitro release, increased permeability, and increased permeation. TBLs are thought to be superior to transferosomes and bilosomes for drug delivery through the intranasal mucosa. Additionally, these unique vesicles were fabricated with an aim to create transbilosomes by combining the benefits of transferosomes and standard bilosomes in a single formula. Additionally, nanovesicle surface engineering becomes very important to potentiate and attenuate a potential payload.

This study was carried out to investigate the prospective role of implementing (HA), a main component of the ECM, as the natural legend and a surface-bound targeting moiety (RHAMM), CD44, and ICAM for neural cell surface receptors in brain cells, facilitating special uptake and persuasive therapeutic efficacy.<sup>10,42</sup> Thus, HA-decorated transbilosomes (TBLs) were developed and fabricated to enhance CIT permeation across nasal mucosa, distribution, controlled-release characteristics, specific brain targeting, and modulation of mucoadhesion of the coated formula by further incorporation of mucoadhesive and thermosensitive gelling system with extensive nasal mucociliary transit time. A temperature-induced in situ gelling system that turns into a gel appearance at body temperature was fabricated

utilizing poloxamer 407 and poloxamer 188 combined with mucoadhesive polymer Carbopol 971 to boost the intranasal residence time of the thermogelling system.

It was found that the earlier literature lacks satisfactory data about any targeting CIT delivery to the brain. Thus, this study was established to achieve two main targets. The first one was to formulate CIT-HA\*TBLs thermogel for intranasal delivery of CIT to the brain. The Second target was to assess the in vivo efficiency of the CIT-HA\*TBLs thermogel compared to (CIT solution, control thermogel, UN hyaluronated CIT-TBLs, and HA-TBLs) using a rat model of AlCl<sub>3</sub>-induced AD.

## Materials and Methods

### Materials

Citicoline sodium (CIT) was obtained as a kind gift from GLOPAL NAPI Pharmaceutical (6th of October City, Egypt). Lipoid AG, (PHOSPHOLIPID GmbH Nattermannallee1 Sennweidstrasse44, CH-6312Steinhausen, and Switzerland) kindly supplied Phospholipon 90 G (PL 90 G). The following items were bought from Sigma-Aldrich (St. Louis, MO, USA): cellulosic membrane (12,000–14,000 kDa molecular weight cut-off), sodium deoxycholate (SDC), hyaluronic acid (HA), Poloxamer 407 (PL 407), Poloxamer 188 (PL 188), Carbopol 971 (CAP971), and cholesterol (CHO). Methanol HPLC grades, chloroform and Cetalkonium chloride (CKC), and sorbitan monostearate (Span 60) were purchased from Across Organics (Cairo, Egypt). Aluminum chloride (molecular weight: 133.332 g/mol) was purchased from El-Gomhouria Chemical Company (Cairo, Egypt). The microRNA-137 (miR-137) qRT-PCR Master Mix for a quantitative real-time polymerase chain reaction was obtained from Thermo Fischer Scientific Co., Massachusetts, USA (Cat. No. 4427975). The ELISA kits were purchased for Nuclear Factor Kappa B (NF-κB) and reduced to Malondialdehyde (MDA) from My BioSource Co., San Diego, California, USA (Cat. No. MBS268427 and MBS453975, respectively). The anti- amyloid-beta (Aβ<sub>1-42</sub>) primary antibody for the immunohistochemical assay was obtained from Thermo Fischer Scientific Co., Massachusetts, USA (Cat. No. BS-0107R). All of the other reagents were of analytical grade.

### Method

#### Experimental CIT Design

A 3<sup>3</sup> Box–Behnken Design Expert<sup>®</sup> (Version 13, Stat-Ease Inc. Minneapolis, MN) was utilized to prepare 15 formulae of CIT-TBLs where the independent variables were the amount of PL90G (X<sub>1</sub>), SP<sub>60</sub> (X<sub>2</sub>), and SDC (X<sub>3</sub>). According to Table 1, the dependent variables were the following: particle size (Y1), zeta (Y2), EE% (Y3), % Cumulative drug released for 8h (Y4), and Cumulative drug permeated through nasal mucosa for 24h (Y5).

**Table 1** The Independent Variables, Their Respective Levels, and the Summarize Statistics Model of Box–Behnken Design Used for Optimization of CIT Transbilosomes

Variable			Level Used				
			Low (-1)	Medium (0)	High (+1)		
Independent variables (Factors)							
X <sub>1</sub> = PL amount (w/w)			100	200	300		
X <sub>2</sub> = SP60 amount (w/w)			20	35	50		
X <sub>3</sub> = SDC amount (w/w)			10	15	20		
Dependent variables	R2	Adjusted R2	Predicted R2	Constraints	p value	F value	Adequate precision
Y1: Vesicle size (nm)	0.9954	0.9872	0.9275	Minimize	0.0001	49.39	17.588
Y2: Zeta potential (mV)	0.9978	0.9939	0.9675	Maximize	0.0003	121.17	35.892
Y3: EE%	0.9889	0.9689	0.8225	Maximize	0.0002	253.30	50.733
Y4: Q8h (%)	0.9985	0.9959	0.9906	Maximize	0.0001	374.66	62.708
Y5: Q24 (μg/cm <sup>2</sup> )	0.9973	0.9923	0.9571	Maximize	0.0001	202.28	44.315

**Abbreviations:** PL 90 G, Phospholipon 90 G; SP60, Span 60; SDC, sodium deoxycholate; EE%, entrapment efficiency percent; Q8h, cumulative release after 8 h; Q24, cumulative amount permeated/unit area in 24 h.

## Preparation of CIT-TBLS Formulae

Different CIT-TBLS formulae were prepared according to the technique of thin-film hydration with some modifications.<sup>43</sup> Briefly, the mixed lipid consisting of PL 90G, SP<sub>60</sub>, and constant weight of CHO (10 mg) was added to bile salt and dissolved in 15 mL chloroform: methanol (2:1) in a round-bottom flask. The produced organic solution was evaporated at 60°C for 30 min under reduced pressure using a rotary evaporator (Stuart rotary evaporator, RE300, Wolf Laboratories, North Yorkshire, UK, with Stuart vacuum pump, RE3022C, Wolf Laboratories, North Yorkshire, UK), until a thin, entirely dry film was created. The resulting film was maintained for 2 h in a desiccator under vacuum for complete removal of traces of solvent.

The dried lipid film was then completely hydrated by adding 10 mL of SNES pH 5.5 containing 50 mg CIT and the flask was allowed to rotate at 100 rpm for 1 hour under normal pressure. The suspension was preserved at 4 °C for complete hydration process through phospholipid swelling (maturation), resulting in large multilamellar vesicles.<sup>44,45</sup> This step increases the loading of the CIT medication into the vesicle, also keeping the vesicle overnight aids in stabilizing it.<sup>46</sup> The size of the multilamellar TBLS was subsequently decreased by sonicating the suspension for 30 minutes in a bath sonicator (Sonix TVs-series ultrasonicator, Sonix IV Ultrasonic Cleaning Systems, North Charleston, SC).<sup>47,48</sup>

Table 3 details the components of these formulae. The optimized formula was integrated and coated by HA (1.5% w/v),<sup>38</sup> in 10 mL of SNES pH 5.5 containing 50 mg CIT, and in the case of coating, the charge inducer (CKC) was requisite for use. For the preparation of the HA formula, CIT-TBLS were decorated with HA by which (CIT-HA\*TBLS) formed via electrostatic interaction between positively charged CKC in the organic phase and negatively charged HA in the aqueous phase. The decorated formula was then kept in the refrigerator for further studies.<sup>48</sup>

## In vitro Characterization of CIT-TBLS

### Size and Zeta Potential Determination

The average size distribution and polydispersity index (PDI) of CIT-TBLS were evaluated by the dynamic light scattering method (DLS) using a Malvern Mastersizer.<sup>49,50</sup> Briefly, the TBL samples (0.1 mL) were diluted 100 times using deionized water to obtain an efficient light scattering intensity; then, the temperature was maintained at 25°C with a 90° scattering angle. Determination of surface charge was performed using the same instrument. The approach analyzes the electrophoretic motion of the particles in an electrical field using the same diluted sample.<sup>51</sup>

### Determination of Encapsulation Efficiency (EE %) of CIT-TBLS

The ultracentrifugation technique was applied to determine the EE% of the CIT-TBLS suspension. The samples were kept at 4 °C overnight for maturation of the TBLS vesicle and then centrifuge at 14,000 rpm for 3hrs at 4°C using a refrigerated centrifuge (SIGMA 3–30K, Steinheim Germany).<sup>52</sup> The free drug (supernatant) was separated from TBL pellets and the amount of entrapped CIT was analyzed spectrophotometrically for the concentration of CIT (Jasco V-530, Japan) at λ<sub>max</sub> 270 nm. Drug EE% was calculated according to the following equation:

$$\text{CIT EE\%} = \frac{\text{Initial CIT amount} - \text{CIT amount in the supernatant}}{\text{Initial CIT amount}} \times 100 \quad (1)$$

### In vitro Release Study of CIT-TBLS

The diffusion analysis was performed according to the dialysis method using vertical diffusion Franz cells with an effective diffusion area of 5 cm<sup>2</sup>.<sup>53</sup>

TBLS' suspension of different formulae equivalent to 3mg drug was placed in the donor compartment. A 50mL of SNES pH 5.5 was utilized as a receptor medium.<sup>54</sup> A magnetic stir bar was used to agitate the receptor compartment, which was kept at 37°C and 100 rpm. A cellulose dialysis membrane with a molecular weight cutoff of 12,000 kDa that had been soaked in the receptor medium overnight was used to separate the donor compartment from the receptor compartment. To maintain a constant volume, 3 mL aliquots were taken out of the sampling port and replaced with an equivalent volume of fresh medium at regular time intervals (0.5, 1, 2, 3, 4, 5, 6, 7, and 8 h).

The CIT content of the aliquots was analyzed using a “UV spectrophotometer” at a  $\lambda_{\text{max}}$  of 270 nm. The analysis was repeated three times and the percent CIT released was expressed as the mean ( $\pm$ SD). The cumulative percent of CIT released from CIT-TBLs was plotted against time. To identify the CIT release pattern, the data were used with various models of release kinetics such as zero-order, first-order, and Higuchi’s matrix.<sup>55</sup> Using the following equation:

$$\text{Release \%} = \frac{\text{The amount of CIT at the time } t}{\text{The total amount of CIT}} \times 100 \quad (2)$$

### Ex vivo Permeation Study

The ex vivo permeability studies of CIT-TBLs formulae and CIT solution were performed as described above in the in vitro release study under the same conditions using fresh isolated camel nasal mucosa. The mucosa was attained instantly following animal sacrifice in a nearby slaughterhouse and utilized as a model membrane because its morphology and permeability are similar to those of the human nose.<sup>56</sup> The dominant nasal concha was recognized, dissociated from the nasal membrane, and allowed to acclimate for 30 min in PBS pH 6.4.<sup>57</sup> Different CIT-TBLs formulae equivalent to (3 mg of CIT) were added to the superior mucosal surface (5cm<sup>2</sup>) and placed into receptor media. The temperature of the receptor chamber containing 50 mL of PBS pH 6.4 is controlled at 37 $\pm$ 0.5°C under continuous stirring with the magnetic bar at 100 rpm, in a way that the surface of nasal mucosa just flushes the diffusion fluid. The experiment was carried out under a non-occlusive state. At regular times, formulae samples were taken out of the receptor compartment (1, 2, 3, 4, 5, 6, 8, 10, 12, and 24 h); then, the receptor chamber was recompensed with equal volumes of fresh milieu. The withdrawn samples were filtered through a 0.45- $\mu$ m Millipore filter and finally measured at 270 nm using a spectrophotometer. For each formula, the cumulative amount of CIT drug permeated per unit area ( $\mu$ g/cm<sup>2</sup>) was plotted versus time (h).

The permeation parameters involving  $Q_{24}$  in  $\mu$ g/cm<sup>2</sup>, the lag time in min, permeability coefficient (KP) in cm/h, and drug flux (Jss) in  $\mu$ g/cm<sup>2</sup>h were computed for each formula and the control CIT solution. Additionally, the enhancement index (EI) was calculated applying the following equation:

$$EI = \frac{K_{\text{pof CIT-TBLs}}}{K_{\text{pof CIT control solution}}} \quad (3)$$

### Optimization of CIT-TBLs

The optimization process was carried out following three-factor, three-level Box–Behnken design as illustrated in Table 1 using Design Expert<sup>®</sup> (Version 13.0, Stat-Ease Inc. Minneapolis, MN). A design matrix comprising 15 experimental runs was used in TBLs formulae (Table 3). The amount range and ingredient of independent variables were chosen upon preliminary research experiments and data collected from the literature review. The nonlinear computer-engendered quadratic model was given the following equation:

$$y = b_0 + b_1X_1 + b_2X_2 + b_3X_3 + b_{12}X_1X_2 + b_{13}X_1X_3 + b_{23}X_2X_3 + b_{11}X_1^2 + b_{22}X_2^2 + b_{33}X_3^2 \quad (4)$$

where Y is the dependent measured response associated with each factor-level combination;  $b_0$  is an intercept;  $b_1$ ,  $b_2$ , and  $b_3$  are regression coefficients;  $b_{12}$ ,  $b_{13}$ , and  $b_{23}$  are interaction coefficients, while  $b_{11}$ ,  $b_{22}$ , and  $b_{33}$  represent interaction and quadratic coefficients computed from the resultant experimental values of response from experimental runs; and  $X_1$ ,  $X_2$ , and  $X_3$  are coded intensity levels of the independent variables. While the amount of all PL90G ( $X_1$ ), Sp<sub>60</sub> ( $X_2$ ), and SDC ( $X_3$ ), which is a process independent variable introduced as low (−1), medium (0), and high (+1), as described in Table 1.

## Evaluation of Optimized CIT-TBLs After Hyaluronated with HA

### Determination of the Physical Properties

The same procedures previously described for the characterization of un-hyaluronate TBLs in the determination of EE%, VS, ZP, PDI, Q8h, and Q24h section were adopted.

### Morphology Study of Optimized CIT-TBLs and CIT-HA\*TBLs

The morphology and size of optimized CIT-TBLs and CIT-HA\*TBLs were examined using a transmission electron microscope (TEM-HR-2100, Joel, JAPAN).<sup>58</sup> The freshly prepared samples were negatively stained with 2% phosphotungstic acid that was previously diluted with double-ionized water and then applied onto a 400-mesh copper grid coated with carbon film. Finally, the samples were left to dry at room temperature to allow adherence of CIT-HA\*TBLs and CIT-TBLs formulae to the carbon film. TEM observation was carried out at an accelerating voltage of 200 kV and the photographs were taken at suitable magnifications.<sup>40</sup>

### Differential Scanning Calorimetry (DSC) of the Optimized CIT-HA\*TBLs

The thermal properties of the plain drug (CIT), excipients (PL90G, SP 60, SDC, CHO, CKC, and HA) drug–excipients mixture (physical mix in a ratio of 1:1), and the optimized CIT-HA\*TBLs formula were assessed using DSC (DSC 50 Shimadzu, Kyoto, Japan). First, 5 mg samples were placed, and hermetically sealed in flat crucible aluminum pans, and then they were heated at 25–400 °C at a scanning rate of 10 °C/min under inert nitrogen flow at 25 mL/min.<sup>32</sup> DSC thermograms were recorded.<sup>59</sup>

### Physical Stability of the Optimized HA\*CIT-TBLs

The optimized CIT-HA\*TBLs were stored for 30, 60, and 90 days in a glass vial at 4 °C, and then the VS, Zp, and EE% were assessed.<sup>60</sup>

### Preparation of Optimized CIT-HA\*TBLs in Thermogel

A thermosensitive gel system was created using the optimized CIT-HA\*TBLs formula. Poloxamer 407 (22% w/v), Poloxamer 188 (10% w/v), and Carbopol 971 (1% w/v), were all included in the thermogel base combination.<sup>61</sup> The cold procedure, as previously described, was used to create the gel base.<sup>62,63</sup> An accurately weighed amount of the three polymers, and preservatives (mixture of 0.1% methyl paraben and 0.01% propyl paraben) were sprinkled in the calculated amount of CIT–HA\*TBLs (5 mg CIT/g). The mixture was stirred using a magnetic stirrer to ensure complete polymers' solubility at room temperature until no lumps were observed then stored overnight at 4°C to ensure complete swelling and form in situ gel. The previous technique was applied to form control in situ gel (free CIT without HA\*TBLs vesicles) by sprinkling the polymeric ingredients on a solution of CIT dissolved in SNSS.

### Measurement of the Sol-to-Gel Transition Temperature

The sol-to-gel phase transition temperature (gelation temperature) was measured for all the prepared CIT-HA\*TBLs thermogel formulae according to the technique described previously by Mansour et al.<sup>64</sup> An aliquot of 2 mL of the primed dispersion was transported to a test tube in a thermostatically digital water bath at 15°C and wrapped well by the parafilm membrane. The temperature of the bath was elevated in increments of 3°C (or 0.5°C in the region of Sol–gel) and left to equilibrate at each new setting. The thermogel samples were examined for gelation, which was thought to have occurred when the meniscus would no longer move upon orientated to 90°. All measurements were done in triplicates.

### Rheological Properties Determination

The rheological properties of the produced thermogel formulae were determined utilizing Cone and Plate programmable viscometer (DV-III Ultra viscometer, RV model, Brookfield, USA). A sample (0.5 gm) of the tested formula was applied to the lower plate of the viscometer. The viscosities were measured at two different temperatures 25±0.5°C and 37±0.5°C by circulating bath connected to the viscometer-using spindle 52 at a shear rate ranging from 20 to 200 S<sup>-1</sup>. The viscosities, as well as the area of hysteresis loops, were determined. Using the trapezoidal method, the area of the hysteresis loops was calculated. The area under the lower curve was then subtracted from the area under the upper curve. Farrow's equation was applied to examine how different gel bases flowed.

$$\log G = N \log F - \log \eta \quad (5)$$

To determine the value of N, which represents the departure from Newtonian law, log G was plotted against log F. If N is smaller than 1, dilatant flow is present (shear rate thickening).<sup>65</sup>

## Dissolution and Permeation Studies of Thermogel

A 0.5 gm of intranasal thermogel and control gel (equivalent to 5 mg CIT) were utilized in the in vitro release and the ex vivo permeation studies using the same procedure as described above.

## In vivo Study

### Animals

The Ethical Review Board of the Faculty of Pharmacy at South Valley University, Qena, Egypt (acceptance D20-21) permitted the experimental process. The experiment was performed on adult male Wistar rats weighted 180–200 g. Rats were maintained in an air-conditioned ( $25 \pm 1^\circ\text{C}$ ) pathogen-controlled animal room for 2 weeks for adaption before being subjected to laboratory tests with free access to standard forage and tap water ad libitum. The study followed the National Institute of Health's (NIH) Guide for the Care and Use of Laboratory Animals (Publication 85–23, modified 1985) guidelines.

### Experimental Design

The experiment was carried out on seven weight-matched groups consisting of 8–10 rats. The first group was maintained as a standard normal control received only vehicle tween 80. The second group was kept as a positive control group and received aluminum chloride ( $\text{AlCl}_3$ ) intra-peritoneal for 6 weeks in dose (100 mg/kg/i.p).<sup>66,67</sup> Treatment groups received intranasal-tested agents the CIT solution and the freshly prepared thermogel as follows: Group 3 received a CIT solution, Group 4 received CIT control thermogel, Group 5 received CIT-TBLs thermogel, Group 6 received CIT-HA\*TBLs thermogel, and Group 7 received HA\*TBLs thermogel all treatment received for consecutive 2 weeks in dose (0.9mg/kg).<sup>68,69</sup> The doses of test agents were determined with pilot trials guided by the published literature. For the intranasal application of thermogel, rats were held horizontally at a 45-degree angle. Then, the animal's back was supported by the palm of the manipulator's hand, and the skinfold of the neck was fixed between the thumb and the index finger. The thermogel was administered with a micropipette as a small drop covering both nostrils at the end of administration, the rats were returned to their home cage.<sup>70–72</sup>

At the end of the experiment, animals were sacrificed via cervical dislocation followed by separation of the brain immediately, and hippocampus excision was then cleaned with iced saline for biochemical, histopathological, and immunohistopathological examination (Figure 1).

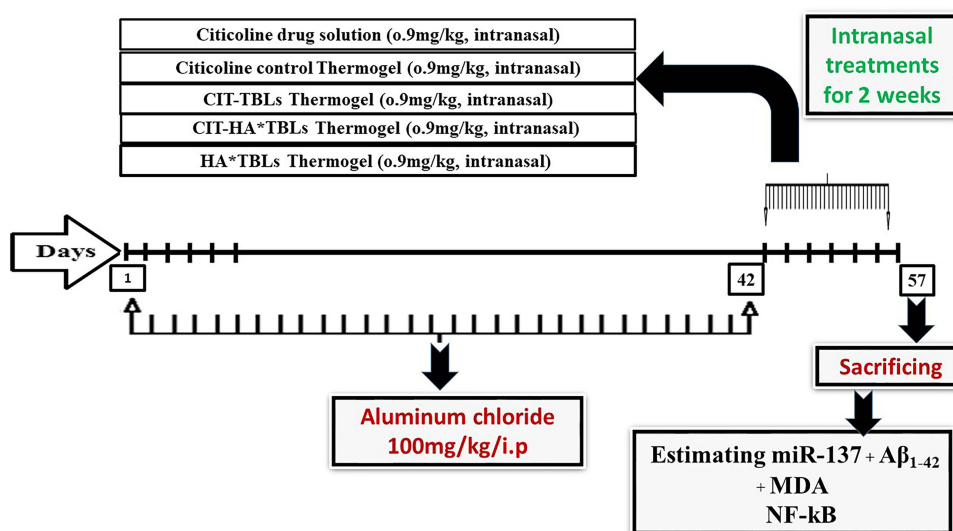


Figure 1 Experimental design of in vivo study.

## Tissue Sampling

Rats were sacrificed by cervical dislocation, the skull was opened, and the brain of each rat was promptly extracted and cut mid-sagittal into two hemispheres. One cerebral cortex hemisphere was cleansed with ice-cold saline to eliminate blood, promptly retained in Eppendorf tubes, embedded in liquid nitrogen, and stored at  $-80^{\circ}\text{C}$  till the time of real-time PCR (qRT-PCR) analysis for miRNA-137. The other cerebral cortex hemisphere was preserved in 10% neutral buffered formalin to be fixed until the histological investigations and immunohistochemistry test of  $\beta$ -amyloid plaques A $\beta$ 1-42.

## ELISA of Tissue Biomarkers

Cerebral cortex hemisphere tissue levels of MDA and NF- $\kappa$ B were measured using ELISA test reagent kits and ELISA Processing System (The prepared reaction mix samples were applied according to the manufacturing protocol and according to the sandwich technique described earlier.<sup>73</sup> StepOne Applied Biosystems, Foster City, USA).

## Quantitative Real-Time Polymerase Chain Reaction (qRT-PCR)

Quantification of miRNA-137 in the hippocampus was determined using the relative gene expression technique of qRT-PCR, which used actin, a housekeeping gene, as an internal reference and the 2Ct method to compute fold changes in the target gene from normal rats as a baseline.<sup>74,75</sup> Following the manufacturer's instructions, the total RNA purification kit extracted the pure RNA from the separated hippocampus after homogenization with a lysis solution. It was done by loading the RNA onto the purification column, which was then eluted with pure RNA under low-ionic strength conditions. The purity was confirmed using UV-Vis-spectrophotometer Q5000 (Quawell Technology, Inc., CA, USA) at OD 260/280 nm and the nanodrop method. The reverse transcription process was used following the manufacturer's instructions to convert RNA into complementary DNA (cDNA). Specific gene primers, whose sequences are provided in Table 2, were used to build the 2X Maxima SYBR Green/ROX qRT-PCR Master Mix, which was used under the manufacturer's instructions and to quantify the expression of genes.<sup>76</sup>

## Histopathological Study

Cerebral cortex hemisphere tissue slides were prepared as indicated by Bancroft and Stevens for histological investigation using conventional hematoxylin and eosin staining.<sup>77</sup> In brief, firstly tissues was fixed in a 10% buffered formalin solution to prepared tissues for histopathological evaluation. After ensuring tissue stiffening, tissues were dehydrated in graded ethyl alcohol (50, 70, 95, and 100%) for 2 hours each and then dripped in a paraffin wax three times for 2 hours each time. Paraffin blocks were then used to prepare sections of 4 $\mu\text{m}$  thickness cut using the Leica microtome. Finally, sections were deparaffinized and stained properly with hematoxylin and eosin to be examined under a light microscope with the aid of a pathologist.

## Immunohistochemically Assay

Tissue amyloid-beta plaques, A $\beta$ 1-42, were detected using the Immunohistochemically technique reported previously by Merz et al.<sup>78</sup> The procedure involved incubating primary antibodies against amyloid plaques, A $\beta$ 1-42 then with secondary antibodies and diaminobenzidine/H<sub>2</sub>O<sub>2</sub>. Histopathology has counterstained slide sections with hematoxylin before the slides were inspected under a light microscope.

## Statistical Analysis

Statistical analyses of biochemical estimations were performed using one way analysis of variance test followed by Tukey-Kramer multiple comparison test, while statistical analysis of the assigned scores in the histopathological study was performed using the chi-square test using statistical package for social sciences (SPSS; version 19.0) computer

**Table 2** Primers Sequence of Mi RNA 137 Gene

Gene	Forward Sequence	Reverse Sequence
Mi RNA 137	GGCGGCATTGCACTTGTCTCG	GTCGAGGGTCCGAGGTATTCCG
GAPDH	TGGATTTGGACGCATTGGTC	TTTGACTGGTACGTGTTGAT

software program (SPSS Inc., Chicago, Ill., USA), with the value of  $p < 0.05$  considered statistically significant. Data are expressed as means of 6–10 values  $\pm$ SEM.

## Results and Discussion

### Preparation and Optimization of CIT-TBLs

Initially, preliminary screening and critical statistical analysis were investigated to explore the impacts of different variables on the TBLs formulae such as the amount of (lipid, surfactant, bile salt, drug), a hydration medium, and time as well as sonication time. All variables were established to obtain an appropriate size of TBLs with the highest EE%. TBL vesicles were obtained using PL incorporated with cholesterol as lipid phase and SP 60 as a surfactant to obtain higher EE%<sup>79,80</sup> and increase the stability of nanovesicles.<sup>81</sup> SDC was used as an edge activator at a different amount. As regards the initial survey, the vesicle preparation was perfectly achieved when these conditions involved 50 mg of CIT, 10 mg of cholesterol, chloroform:methanol ratio (2/1) as an organic solvent, and SENS pH 5.5 as a hydration medium. Hydration for 1 h and sonication for 30 min were sufficiently enough for nanovesicles' formation. The different formulae of the TBLs were prepared following the thin-film hydration process using the various amount of PL, SP<sub>60</sub>, and SDC and characterized for appropriate physicochemical attributes. In order to investigate the impact of independent variables on dependent ones, the Box–Behnken design was created (Table 3). Regression equations and 3D-response surface plots were utilized to further clarify the link between the dependent and independent variables. In the regression equation, a positive sign denotes a synergistic impact and a negative one an antagonistic one. The 3D-response surface plots exhibit the effect of two independent variables after fixing the third one at the medium-level value.<sup>82</sup> The signal-to-noise ratio was calculated with sufficient precision to ensure that the model could be used to explore the design space.<sup>83</sup> It is preferable for all dependent parameters (EE percent, VS, ZP, Q8 and Q24h) to have a ratio greater than 4 (Table 1). The adjusted and anticipated  $R^2$  values should be comparable to each other in order to have a fair agreement, which was achieved for all parameters (Table 1). The experimental run is listed and calculated along with the measured parameters (Table 3).

**Table 3** Observed Response in Box–Behnken Experimental Design of CIT-Loaded TBLs

Formula	Independent Variables				Dependent Variables				PDI
	X <sub>1</sub> : PL 90G Amount (w/w)	X <sub>2</sub> : SP60 Amount (w/w)	C: SDC Amount (w/w)	Y <sub>3</sub> : EE%	Y <sub>1</sub> : Vesicle Size (nm)	Y <sub>2</sub> : Zeta Potential (mV)	Y <sub>4</sub> : Q <sub>8h</sub> (%)	Y <sub>5</sub> : Q <sub>24</sub> ( $\mu$ g/cm <sup>2</sup> )	
TBLs 1	300	35	10	72.35 $\pm$ 3.80	209.90 $\pm$ 19.33	-32.90 $\pm$ 1.00	78.24 $\pm$ 2.27	495.65 $\pm$ 26.72	0.329
TBLs 2	300	20	15	70.45 $\pm$ 2.81	194.84 $\pm$ 7.05	-30.9 $\pm$ 4.30	73.13 $\pm$ 1.95	455.61 $\pm$ 22.41	0.106
TBLs 3	100	50	15	50.81 $\pm$ 3.72	371.72 $\pm$ 25.29	-21.91 $\pm$ 7.60	50.43 $\pm$ 2.51	296.12 $\pm$ 16.92	0.103
TBLs 4	100	35	10	50.38 $\pm$ 4.95	345.30 $\pm$ 22.59	-20.34 $\pm$ 9.41	45.45 $\pm$ 2.34	244.97 $\pm$ 16.51	0.268
TBLs 5	100	35	20	48.67 $\pm$ 2.35	343.4 $\pm$ 13.03	-20.9 $\pm$ 3.20	49.83 $\pm$ 2.56	267.53 $\pm$ 15.76	0.226
TBLs 6	200	50	10	52.64 $\pm$ 4.72	305.1 $\pm$ 11.01	-26.7 $\pm$ 6.25	65.79 $\pm$ 2.01	424.81 $\pm$ 19.49	0.192
TBLs 7	200	20	20	52.24 $\pm$ 3.89	226.65 $\pm$ 8.77	-22.93 $\pm$ 6.95	58.27 $\pm$ 1.97	386.72 $\pm$ 24.97	0.329
TBLs 8	300	35	20	71.62 $\pm$ 3.65	207.42 $\pm$ 14.00	-35.43 $\pm$ 7.61	84.34 $\pm$ 2.54	512.67 $\pm$ 38.23	0.131
TBLs 9	100	20	15	45.53 $\pm$ 3.35	332.31 $\pm$ 17.86	-18.50 $\pm$ 8.94	42.56 $\pm$ 2.98	240.43 $\pm$ 12.01	0.246
TBLs 10	300	50	15	75.35 $\pm$ 3.13	263.9 $\pm$ 10.69	-38.3 $\pm$ 5.56	87.25 $\pm$ 3.97	538.78 $\pm$ 21.10	0.243

(Continued)

Table 3 (Continued).

Formula	Independent Variables				Dependent Variables				PDI
	X <sub>1</sub> : PL 90G Amount (w/w)	X <sub>2</sub> : SP60 Amount (w/w)	C: SDC Amount (w/w)	Y <sub>3</sub> : EE%	Y <sub>1</sub> : Vesicle Size (nm)	Y <sub>2</sub> : Zeta Potential (mV)	Y <sub>4</sub> : Q <sub>8h</sub> (%)	Y <sub>5</sub> : Q <sub>24</sub> (µg/cm <sup>2</sup> )	
TBLs I1	200	35	15	49.98± 2.26	241.62± 9.26	-24.12±3.60	62.35± 4.65	407.55± 20.91	0.080
TBLs I2	200	20	10	51.95± 3.59	234.9± 18.96	-22.12±5.36	54.63±2.87	376.65± 17.42	0.382
TBLs I3	200	50	20	51.29± 2.75	285.72± 10.45	-27.5± 2.76	69.67± 3.99	443.92± 21.98	0.250
TBLs I4	200	35	15	50.22± 2.76	242.5± 20.44	-24.26 ±4.80	62.78± 3.62	408.92± 19.61	0.078
TBLs I5	200	35	15	52.62±2.98	243.4± 22.84	-24.52± 8.42	60.59± 4.98	411.56± 22.50	0.113
TBLs OPTI	300	43.97	20	72.92	220.94	-36.379	85.41	528.43	
Observed values				73.32	228.583	-37.619	88.41	530.39	
Predicted values									

**Note:** Data are mean values (n = 3) ± SD.

**Abbreviations:** PL, Phospholipon 90 G; SP60, Span 60; SDC, sodium deoxycholate; EE%, entrapment efficiency percent; Q<sub>8h</sub>, cumulative release after 8 h (%); Q<sub>24</sub>, cumulative amount permeated/unit area in 24 h; PDI, polydispersity index; BLs OPTI, optimized transbilosomes.

## In vitro Characterization of CIT-TBLs

### Size and Zeta Potential Determination

Nano platform-based medicine can provide great opportunities to enable drugs to reach their target sites, either passively or actively.<sup>84</sup> Table 3 shows the vesicle size values of the formulated CIT-TBLs as the z-average diameter, which represents the mean hydrodynamic diameter of the lipid vesicles.<sup>85</sup> The CIT-TBLs were in the nanoscale range, as their VS ranged between 194.8± 7 and 371.7± 25. nm. In Figure 2A, 3D response surface plots are used to graphically depict how PL (x<sub>1</sub>), SP 60 (x<sub>2</sub>), and SDC (x<sub>3</sub>) quantity affect the VS of the TBLs. The size values were subjected to Statistical polynomial analysis and the quadratic model was selected (p<0.0001). Equation 6 shows the quantitative effects of the independent variables on the VS of the TBLs formulae.

$$VS = 142.51 - 169.58X_1 + 24.69X_2 - 3.99X_3 - 2.58X_1X_2 - 0.14X_1X_3 - 2.73X_2X_3 + 25.83X_1^2 + 12.35X_2^2 + 8.17X_3^2 \quad (6)$$

The VS was directly dependent on the effect of PL (x<sub>1</sub>); as the amount of PL was raised from 100 to 300mg unpredictably, decreasing in the mean VS may be attributable to the availability of more surface area at a high level of PL amount resulting in an accommodating more of CIT into the vesicle bilayer.<sup>86,87</sup> The high amount of drug captured in vesicles revealed better packing of the vesicular membrane and a consequent size reduction.<sup>88</sup> These findings are similar to those of a previous study.<sup>36</sup> As well, the VS was found to significantly increase with increasing Span 60 amount (X<sub>2</sub>) (p = 0.0012). These findings are in line with previous results, where combining higher content of Span 60 led to higher EE percentage of drug consequently, the whole VS of CIT-TBLs was increased. This may be attributable to the interposition of SP 60 in the bilayer membrane, with the polar head towards the hydrophilic phase.<sup>89,90</sup> However, the increase in flexibility and decrease in membrane tension between the aquatic and lipid aspects caused by the reduction in VS and the augmentation of SDC in the nanovesicle lipid bilayer resulted in the creation of smaller droplets at the nanoscale.<sup>91</sup> Our findings are consistent with those of Guan et al, who claimed that the smallest ratio of PL: SDC was the main contributor to the production of small particle size of probiosomes containing cyclosporine A.<sup>92</sup> Additionally, our findings are consistent with those of Ahad et al, who revealed that a rise in the PL: SDC ratio resulted in a reduction in the particle size of liposomes containing bile salt.<sup>93</sup>

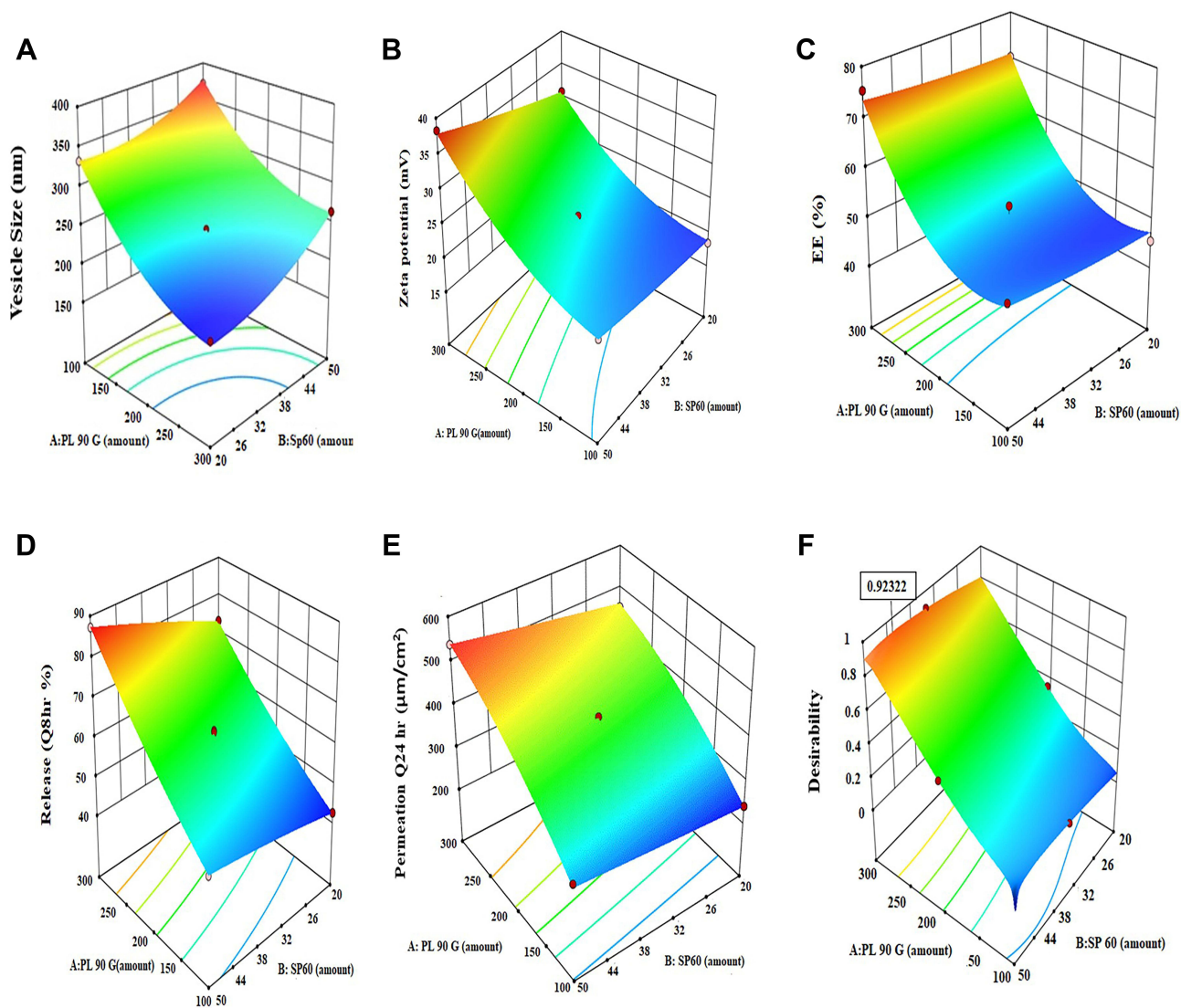


**Figure 2** Response surface plot for the effect of PL amount ( $X_1$ ), Sp60 amount ( $X_2$ ) at the middle levels of the third (SDC amount) on (A) vesicle size (B) zeta potential (C) EE%, (D)  $Q_{8hr}$ , (E)  $Q_{24}$  and (F) desirability of the developed BLs dispersions.

The stability of CIT-TBLs colloidal dispersions can be partially indicated by zeta potential values which is a crucial characteristic that can influence vesicular properties. Due to electrostatic repulsion, it can dramatically prevent the mutual agglomeration, fusion of nanovesicles and enhances its stability. Abdelbary stated that particles are considered stable when the ZP value is around  $\pm 30$  mv.<sup>94</sup> The ZP of the TBLs formulae ranged between  $-18.50 \pm 8.94$  and  $-38.3 \pm 9.56$  mV (Table 3).

$$Z_p = 19.27 - 6.11X_1 - 2.0X_2 - 0.071X_3 + 0.00X_1X_2 - 0.73X_1X_3 + 0.00X_2X_3 - 1.98X_1^2 - 0.65X_2^2 + 0.12X_3^2 \tag{7}$$

Equation 7 shows the quantitative effects of the three independent variables on the ZP of the TBLs formulae. Where  $X_1$  is PL,  $X_2$  is SP 60, and  $X_3$  is SDC. It is found that all the three independent variables had a significant influence on the ZP ( $p = 0.0003$ ) (Figure 2B). The equation shows that TBLs vesicles with the highest PL amount had the greatest ZP.

Although the PL heads are zwitterions and thus are hypothetically unconvicted at a neuter pH, they nevertheless create a negative ZP value in water due to the orientation of the head group and the formation of water layers on their surface.<sup>95</sup> According to Makino et al, charge of a phospholipid bilayer is caused by the orientation of the dipole, which

involves the negative charge of the phosphatidyl molecule and the positive charge of the choline molecule in the head group.<sup>96</sup>

The head group has been shown to be orientated so that the positive choline gathering is inside and the negative phosphatidyl gathering is outside in a medium with low ionic strength, producing a negative surface charge.<sup>95</sup> The results demonstrate that the amount of SP60 significantly affected the ZP values of the CIT-TBLs dispersion ( $P=0.0018$ ). This might be explained by the surfactant-forming vesicles' lipophilicity. Whenever a surfactant's lipophilicity is decreased, the ZP values increase because the surfactant's surface free energy is reduced. This is in harmony with the findings of Abd-Elal et al,<sup>97</sup> who investigated the impact of surfactant type and ratio on zolmitriptan-loaded novosomes. They found that when the ratio of this surfactant was increased from 1:1 (SP 60:oleic acid) to 2:1 (SP 60: oleic acid), the ZP of vesicles dramatically improved in vesicular surface charge from (- 63.77±1.12 mV) to (-68.10±10.18 mV). Similar to this, raising the SDC amount dramatically elevated the ZP values. SDC producing negative surface charges and strong electrostatic repulsions between the particles is a feasible explanation.<sup>97</sup> These findings point to the vesicles' strong stability.<sup>52</sup> When it comes to the polydispersity index (PDI), a value of 0 represents the ideal and uniform population, whereas a PDI that is almost equivalent to 1 suggests extremely polydispersity vesicles.<sup>98</sup> The PDI values in this investigation varied between 0.078 and 0.382, which is indicative of good homogeneity and a restricted particle distribution.<sup>99</sup>

### Effect of Formula Variables on TBLs' EE%

The prospective role of the formulated TBLs to retain a high amount of CIT is critical for its potential manipulation as a successful brain targeting delivery system. The percent of CIT entrapped within the TBLs ranged from 45.53± 3.35% to 75.35± 3.13% (Table 3). Thus, CIT was successfully entrapped in the CIT-TBLs, indicating that lipid-based TBLs can be used as a delivery system for water-soluble drugs. The increase of PL ( $x_1$ ), SP<sub>60</sub> ( $x_2$ ), and SDC ( $X_3$ ) amount on the EE% of the TBLs are graphically illustrated as 3D response surface plots in Figure 2C.

The ANOVA showed that the best-fitted model for assessing the EE% values was a quadratic model. The resulting equation in terms of coded values shows the quantitative effects of the independent variables on EE% of the TBLs formula as follows:

$$EE = 50.15 + 11.80X_1 + 1.24X_2 - 0.4X_3 - 0.095X_1X_2 + 0.25X_1X_3 - 0.41X_2X_3 + 9.55X_1^2 + 0.83X_2^2 + 1.05X_3^2 \quad (8)$$

It was found that EE% values were significantly affected by all three independent variables ( $p<0.0002$ ). The regression coefficients indicate that the PL and SP60 amount had a noticeable positive effect on EE%, while the SDC amount had negative effects on EE%. The impacts of PL and SP<sub>60</sub> amount on EE% at the middle level of the third independent variable (SDC amount) are shown in Figure 2C. Elevating the PL amount from 100 to 300 mg significantly enhanced the EE% ( $p<0.0001$ ), possibly because there was increased space to incorporate the CIT into TBL vesicles.<sup>100</sup> This results in harmony with the study by Singh et al.<sup>101</sup> The increase in Span 60 amount leads to significantly higher enhancement in EE. The outcome is consistent with the research by Singh et al.<sup>101</sup> An increase in Span 60 results in a noticeably bigger improvement in EE. The increase in the quantity of nanovesicles produced with rising Span 60 concentrations could serve as confirmation.<sup>102</sup> The rise in the EE may be related to the large phase transition temperature (50°C) and alkyl chain lengths of Span 60. The drug's permeability into the bilayer of lipid vesicles is increased by Span 60's long alkyl chain, which raises EE. In direct proportion to the surfactant's lower HLB value (Span 60, HLB 4.7),<sup>103</sup> the drug entrapment and stability would rise.<sup>103</sup> These results were consistent with the earlier-reported finding.<sup>104</sup>

Regarding SDC amount ( $X_3$ ), many studies stated that EE percent of TBLs was decreased as the bile salt concentration increased. They explained this finding as a result of the bile salts' fluidizing effects on the bilayer membrane of the vesicles, which cause the loading drug to leak out.<sup>105</sup> Moreover, a high bile salt concentration causes the development of mixed micelles that increase drug solubility in the hydrous milieu throughout preparation, endangering the EE percent.<sup>106,107</sup> In this study, the results are not entirely support these findings, as it is clear that the quantity of SDC increases with a minor decrease in the amount of EE of the drug, and the influence of SDC concentration on EE percent is negligible ( $p = 0.525$ ).

## In vitro Drug Release

In vitro release behavior of CIT-TBLs formulae in comparison with that of control (CIT solution in PBS) are demonstrated in [Table 3](#), and graphically profiled in [Supplementary Figure 1A](#) and [B](#). The effect of the independent variables on Q8h percentage of the prepared CIT-TBLs formulae was confirmed in 3D-graph ([Figure 2D](#)). The data obtained from in vitro release studies proved that the CIT-TBLs could release CIT in a controlled manner. The rate of CIT released from drug solution was significantly higher than the investigated TBLs formulae ( $p < 0.005$ ). Where drug solution pointed out a 99.99% of CIT release in the first 4 h. In contrast, the prepared TBLs formulae could retard the release of CIT to more than 8 h (42.56 –87.25%). The cumulative percentage of CIT released from TBLs after 8 h (Q8h) was subjected to polynomial analysis and the quadratic model was selected; The ANOVA test for the observed Q8h in CIT-TBLs data indicated that the quadratic model was significant and best fitting for the data ([Table 3](#)). The equation of Q8h for CIT-TBLs in terms of coded values is given as follows.

$$Q8h\% = 61.91 + 16.84X_1 + 5.57X_2 + 2.25X_3 + 1.56X_1X_2 + 0.43X_1X_3 + 0.060X_2X_3 + 1.91X_1^2 - 0.47X_2^2 + 0.65X_3^2 \quad (9)$$

The equation discloses that the three examined independent variables elucidated a significant impact on the percentage of in vitro CIT release after 8 h ( $p < 0.0001$ ). Due to the amphiphilic characteristics of PL, an increase in the amount of lipid from 100 to 300 mg resulted in a considerable increase in the percentage of drug release after 8 h ( $p < 0.0001$ ).<sup>108</sup> The high lipid content followed by low VS, as was previously noted in the VS assessment, therefore an increase in the percentage of drug release is expected. The increasing addition of Span 60 to the TBLs formula was also discovered to be associated with a noticeable rise in the CIT release rate. Indeed, the more association of surfactant particles in the formula provides higher deformability, fluidity, and elasticity for the bilayer membrane of the nanovesicles, which is the favored for drug release.<sup>53</sup>

Furthermore, there was a favorable correlation between the amount of medication released from TBLs and the increase in SDC amount. The fluidity effect of SDC, which increases lipid bilayer flexibility and facilitates drug leaking from the vesicles, may be responsible for this action.<sup>109</sup> Linear kinetic analysis of the CIT release data revealed that most CIT-TBLs formulae were the coefficient of correlation value ( $R^2$ ) best fitted with the Higuchi kinetics equation, as the  $R^2$  values predominate over zero-order and first-order kinetics. This indicates the CIT release mechanism by diffusion, as the slow and sustained release of the medication is achieved by its diffusion from the matrix of the TBLs system, as proposed by Higuchi ([Supplementary Table 1](#)).

## Ex vivo Permeation of CIT-TBLs

The diffusion studies provide valuable visions about in vivo performance.<sup>110</sup> The intranasal permeation analysis was performed on CIT-TBLs formulae and CIT solution, the results obtained are shown in [Table 3](#), and graphically profiled in [Supplementary Figure 2A](#) and [B](#). The calculated diffusion parameters for each TBLs formula along with CIT solution are recorded in [Table 4](#). The diffusion parameters including Q24 ( $\mu\text{g}/\text{cm}^2$ ), lag time (min), Kp (cm/h), and Enhancement ratios were used to assess the intranasal permeation capability of the tested TBLs formulae against CIT solution. The permeation analysis proved that the developed TBLs formulae exhibited a significantly higher ( $P < 0.05$ ) nasal permeation compared with the CIT solution containing the equivalent amount of CIT. The permeation of the CIT-TBLs formulae ranged from  $240.43 \pm 12.81$  to  $538.78 \pm 21.15 \mu\text{g}/\text{cm}^2$  ([Table 3](#)), which indicated enhanced permeation compared to the CIT solution ( $118.30 \pm 16.0 \mu\text{g}/\text{cm}^2$ ).

This may have been due to the CIT-TBLs composition involving both phospholipids and edge activators,<sup>48,111</sup> their small VS creating a large surface area for enlarged contact of released CIT with the nasal mucosa surface. The intranasal flux (Jss) of the CIT-TBLs formulae ranged from  $10.32 \pm 0.12$  to  $22.97 \pm 1.83 \mu\text{g}/\text{cm}^2/\text{h}$  compared to only  $5.4 \pm 0.69 \mu\text{g}/\text{cm}^2/\text{h}$  for the CIT solution. The enhancement ratios of the CIT-TBLs formulae compared to the CIT solution ranged from 1.6 to 4.28. Statistical analysis of the Box–Behnken design exhibited that the quadratic model was significant and best fitting for the data. The quantitative impacts of the independent factors on Q24h% of CIT-TBLs are shown in Equation 10 as follows:

**Table 4** Ex vivo Permeation Parameters of CIT-TBLs Formulae versus CIT Solution

Formula No.	Lag Time (min)	Jss ( $\mu\text{g}/\text{cm}^2\cdot\text{h}$ )	Kp (cm/h)	EI
TBLs 1	51.41 $\pm$ 1.53	21.4 $\pm$ 0.19	0.0214 $\pm$ 0.0002	4.02 $\pm$ 0.59
TBLs 2	40.52 $\pm$ 10.48	19.57 $\pm$ 0.28	0.0196 $\pm$ 0.0003	3.66 $\pm$ 0.46
TBLs 3	44.14 $\pm$ 8.29	12.75 $\pm$ 0.75	0.0128 $\pm$ 0.0007	2.4 $\pm$ 0.48
TBLs 4	36.89 $\pm$ 6.44	10.42 $\pm$ 0.21	0.0104 $\pm$ 0.0002	1.64 $\pm$ 0.73
TBLs 5	56.22 $\pm$ 6.31	11.64 $\pm$ 0.14	0.0116 $\pm$ 0.0001	2.18 $\pm$ 0.31
TBLs 6	36.94 $\pm$ 3.82	18.17 $\pm$ 0.23	0.0182 $\pm$ 0.0002	3.14 $\pm$ 0.51
TBLs 7	39.66 $\pm$ 2.06	16.47 $\pm$ 0.36	0.0165 $\pm$ 0.0004	3.09 $\pm$ 0.46
TBLs 8	19.23 $\pm$ 5.56	21.69 $\pm$ 0.23	0.0217 $\pm$ 0.0002	4.07 $\pm$ 0.61
TBLs 9	38.2 $\pm$ 2.76	10.32 $\pm$ 0.12	0.0103 $\pm$ 0.0001	1.93 $\pm$ 0.28
TBLs 10	18.58 $\pm$ 3.89	22.86 $\pm$ 0.18	0.0229 $\pm$ 0.0018	4.28 $\pm$ 0.61
TBLs 11	32.33 $\pm$ 2.94	17.5 $\pm$ 0.161	0.0175 $\pm$ 0.0025	3.28 $\pm$ 0.44
TBLs 12	53.97 $\pm$ 4.55	16.36 $\pm$ 0.03	0.0165 $\pm$ 0.0016	3.08 $\pm$ 0.41
TBLs 13	17.72 $\pm$ 5.39	18.74 $\pm$ 0.15	0.0187 $\pm$ 0.0015	3.51 $\pm$ 0.52
TBLs 14	24.72 $\pm$ 3.75	17.4 $\pm$ 0.14	0.0174 $\pm$ 0.0014	3.26 $\pm$ 0.42
TBLs 15	26.11 $\pm$ 10.53	17.28 $\pm$ 0.29	0.0173 $\pm$ 0.00023	3.24 $\pm$ 0.44
CIT solution	103.43 $\pm$ 10.35	5.4 $\pm$ 0.75	0.0054 $\pm$ 0.0007	–

**Note:** Data are mean values (n = 3)  $\pm$  SD.

**Abbreviations:** Jss, drug flux; Kp, permeability coefficient; EI, enhancement index.

$$\begin{aligned}
 Q_{24h\%} = & 409.34 + 119.21X_1 + 30.53X_2 + 8.59X_3 + 6.78X_1X_2 - 1.38X_1X_3 + 2.26X_2X_3 - 27.21X_1^2 \\
 & + 0.60X_2^2 - 1.93X_3^2
 \end{aligned}
 \tag{10}$$

By inspection of the results, the independent variables significantly improved the Q<sub>24</sub> of CIT-TBLs ( $p < 0.0001$ ) (Figure 2E). All variables had a positive regression coefficient, indicating their positive impacts on diffusion. ANOVA analysis exhibited that lipid amount ( $X_1$ ) and SP60 ( $X_2$ ) were the higher significant predictors of the quantity of drug permeated after 24 h ( $p < 0.0001$ ).

It can be concrete that increasing lipid amount from 100 to 300mg and SP60 from 20 mg to 50 mg (at a low level of SDC) would increase the quantity of CIT permeated across nasal mucosa after 24 h from  $296.12 \pm 7$  to  $538.78 \pm 10.35 \mu\text{g}/\text{cm}^2$ . Two different attitudes have been proposed for the influenced delivery of medicine by nanovesicles.<sup>54,112</sup> The first attitude expects a small vesicle size of CIT-TBLs that resulted in high lipid level and surfactant, which increases the flexibility of the nanovesicles and enables them to pass through the nasal mucosa more easily.<sup>54</sup> The bilayer membrane's extraordinary flexibility allows nanocarriers to squeeze through pores that are much smaller than their sizes.<sup>113</sup> Additionally, phospholipids have a strong affinity for cellular membrane, which helps nanovesicles become more permeable. Second, the vesicles serve as drug nanocarriers, sending whole nanovesicles into the nasal mucosa with drug molecules enclosed inside.<sup>114</sup> According to the third, nanovesicles can operate as penetration enhancers by allowing nanocarriers bilayers to enter the nasal mucosa and create new pores in paracellular tight junctions, improving the fluidity of the mucosa.<sup>115</sup> On the other hand, the permeability coefficient showed a moderately significant improvement after using varied doses (10 mg to 20 mg) of SDC ( $p < 0.0324$ ). This could be due to the ability of SDC to boost the vesicles'

flexibility by altering the bilayer packing characteristics.<sup>52</sup> This would help the vesicles to squeeze easily through the nasal mucosa.<sup>116</sup>

### Selection of the Optimized CIT-TBLs

The optimized TBLs formula was selected by the optimization process of the Box–Behnken design, which generated the requisites of each response variable based on a maximal desirability value of 0.9332 (Figure 2F). This formula was composed of 300mg PL, 43.976mg of SP60, and 20 mg SDC. Optimized TBLs showed a size diameter of  $222.94 \pm 3.42$  with narrow PDI  $0.062 \pm 0.013$  and zeta potential of  $-36.37 \pm 4.75$  mV that provided good stability. Also, optimized TBLs showed EE percentage of  $72.92 \pm 4.13\%$ , CIT release rate of  $85.41 \pm 2.07\%$ , and intranasal flux of  $528.43 \pm 11.65$   $\mu\text{g}/\text{cm}^2/\text{h}$ .

### Evaluation of Optimized CIT-TBILS After Hyaluronated with HA

The insertion of HA produced a little smaller VS ( $178 \pm 8.92$  nm) compared with the un-hyaluronate variants ( $220 \pm 12.67$  nm), which is emphasized by the TEM micrograph in Figure 3A and B.

This phenomenon was explained by Abdelkader et al who stated that the addition of HA reduced the PDI and that increasing the viscosity of the dispersion medium decreased the tendency of nanovesicles to aggregate.<sup>117</sup> This lessening in aggregation resulted in the production of TBLs of smaller size than the hyaluronate TBLs. Regarding PDI, the TBLs dispersion is considered mono-dispersed, as the PDI was  $0.049 \pm 0.012$ , which was less than  $0.062 \pm 0.015$ . In this work, the obtained ZP value of optimized CIT-HA\*TBLs was  $-42 \pm 3.6$  mV, which is on the negative side due to the immobilization of hyaluronic acid to the nanovesicles' surface.<sup>117,118</sup> Additionally, there was a moderately higher CIT entrapment percentage for CIT-HA\*TBLs compared to un-hyaluronate TBLs ( $74.5\%$  vs  $72.92\%$ ). This could be linked to hyaluronic acid, the agent that enhances viscosity. As CIT complexation with PL molecules improves, a modest increase in viscosity is expected to result in a rise in EE percent. This follows the results produced by previous literature.<sup>40,119</sup>

### Transmission Electron Microscopy

TEM was conducted to investigate the morphology of optimized CIT-TBLs and CIT-HA\*TBLs. As observed in Figure 3A and B, the examined sample showed homogeneously, well-identified mono dispersed vesicle with a lipid bilayer without agglomeration. The size of the vesicles measured by Zetasizer was typically following the results obtained using TEM. In addition, a higher magnification demonstrated that the vesicles of CIT-HA\*TBLs exhibited a smooth surface and sharp edges, with the concomitance of a HA coat (darker shade) framing the TBLs. This was following the results produced by previous studies.<sup>40,119</sup>

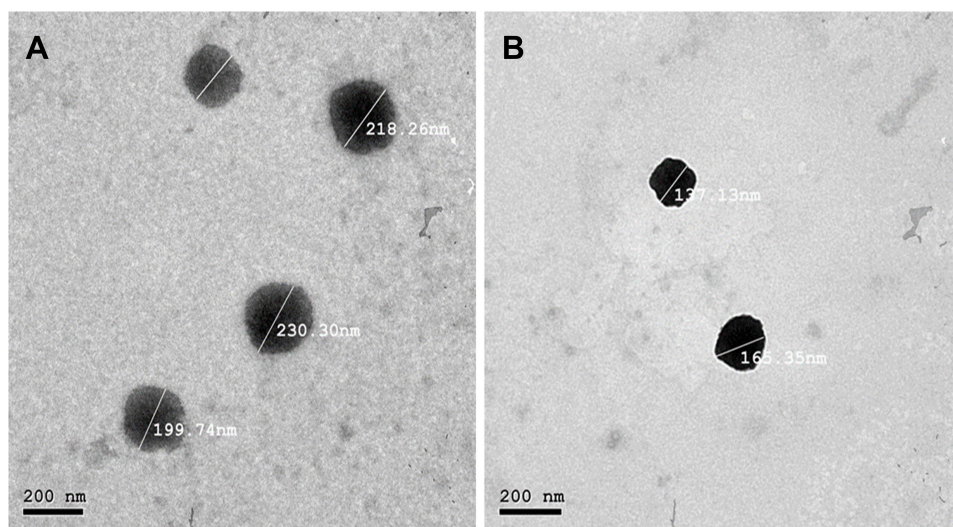


**Figure 3** Transmission electron micrograph of the uncoated CIT-TBLs (A) and coated CIT-HA\*TBLs (B) of optimized formula.

## Release and Permeation Study of CIT-HA\*TBLs

The dissolution and permeation profiles of CIT from the CIT-TBLs and CIT-HA\*TBLs are represented graphically in [Supplementary Figure 3A and B](#). The cumulative release (Q8h percent) and permeation (Q24h  $\mu\text{g}/\text{cm}^2$ ) of CIT from CIT-HA\*TBLs were diminished compared to unhyaluronated TBLs, as shown in Figure S3A and B ( $81.27\pm 3.8\%$ ,  $515.43\pm 12.58\%$  and  $85.41\pm 4.13\%$ ,  $528.43\pm 10.58\%$ , respectively). This slow release in CIT-HA\*TBLs could be due to the presence of an HA-coated on the TBLs surface, which increased the thickness of the TBLs layer and leads to the increase of the diffusion distance. Furthermore, CIT-HA\*TBLs exhibited high negative ZP, which may result in enhanced TBLs stability and diminished TBLs membrane fusion, hence lowering the CIT release out of TBLs.

The above results suggest that CIT-HA\*TBLs would be stable in the blood circulation and would be released at a slow rate at the target site.<sup>118,120</sup>

## DSC Analysis of the Optimized CIT-HA\*TBLs

DSC thermograms of the pure drug (CIT), excipients (PL, SP 60, SDC, CHO, HA, and CKC) drug –excipients mixture (physical mix in a ratio of 1:1), and the optimized CIT-HA\*TBLs formula are shown in [Figure 4](#). The DSC thermograms of CIT exhibited one endothermic peaks at  $270.69^\circ\text{C}$ , as reported previously for CIT<sup>121</sup> ([Figure 4A](#)). Concerning PL 90 G, the thermal analysis shows three endothermic peaks at  $232.21^\circ\text{C}$ ,  $335.03^\circ\text{C}$ , and  $365.48^\circ\text{C}$  ([Figure 4B](#)). SP60 thermograms shows one endothermic peak at  $56.18^\circ\text{C}$  ([Figure 4C](#)).

The thermograph of SDC showed two endothermic peaks at  $87.20^\circ\text{C}$  and  $236.45^\circ\text{C}$  and two an exothermic recrystallization peaks at  $195.02^\circ\text{C}$  and  $335.22^\circ\text{C}$  ([Figure 4D](#)).<sup>122</sup> CHO thermal analysis displays one endothermic peak at  $143.94^\circ\text{C}$  and another exothermic peak at  $352.94^\circ\text{C}$  ([Figure 4E](#)). The thermograms of HA exhibited an endothermic peak at  $82.61.94^\circ\text{C}$  and another two exothermic peaks at  $238.28^\circ\text{C}$  and a peak at  $391.98$  ([Figure 4F](#)). Concerning CKC, the thermal analysis shows one broad endothermic peak started at  $44.71^\circ\text{C}$  and  $195.84$  ([Figure 4H](#)). The thermograms of (the physical Mixture and optimized CIT-HA\*TBLs formula) indicated CIT melting endothermal and exothermal subsidence ([Figure 4G–I](#)). The CIT's distinctive exothermic peak had disappeared, and the endothermic peaks of the surfactant/lipid bilayers had widened and/or altered. This may explain the increased trapping of CIT in the HA\*TBLs in an amorphous state. It also suggests that CIT interacts with the bilayer components, generating many lattice defects.

## Stability Study of CIT-HA\*TBLs Formula

The optimized CIT-HA\*TBLs formula's stability studies were assessed for EE percent, Zp and VS after 30, 60, and 90 days at  $4^\circ\text{C}$  as shown in [Figure 5](#). The formula of CIT-HA\*TBLs showed minor variations in EE percent (reduced from

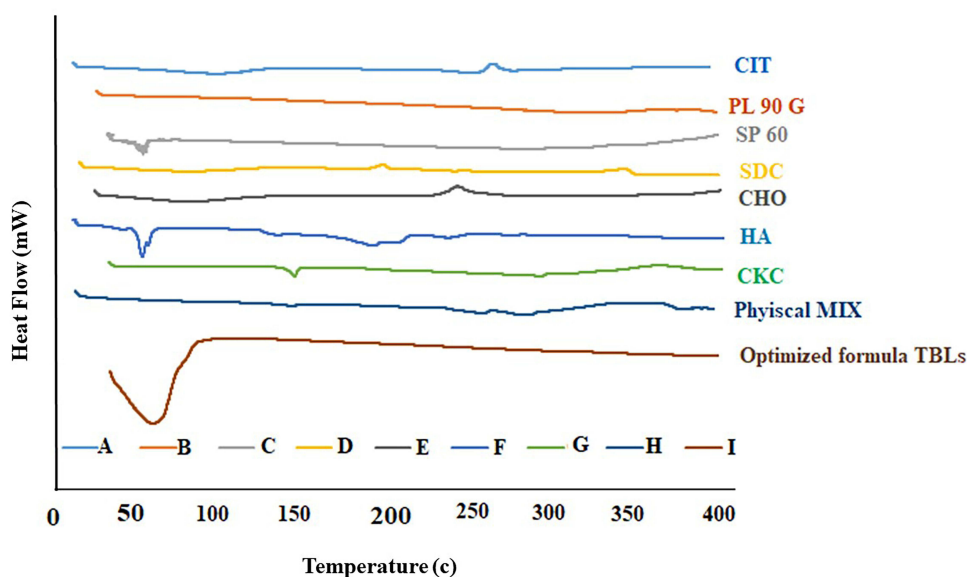


**Figure 4** DSC thermograms of CIT, PL90 G, SP60, SDC, HA, CKC, CHO, physical mixture and CIT-HA\*TBLs-coated nanovesicles formula.

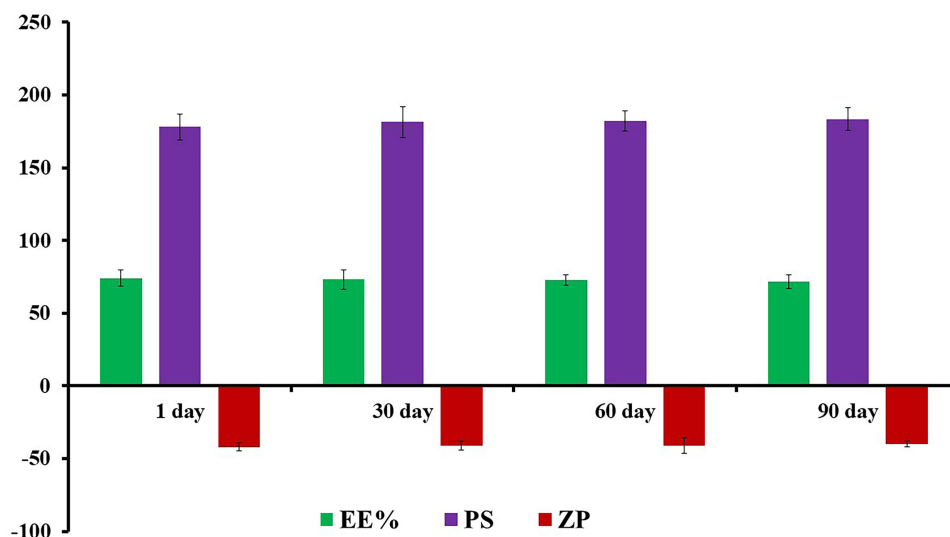


**Figure 5** Effect of storage at 4°C for 3 months on entrapment efficiency (EE), vesicle size (VS) and Zeta potential of the optimized CIT-HA\*TBLs formula.

74.55 to 71.69 4.83) and PS (enlarged from 178.8 to 183.5 nm). Zp changed throughout the stability testing, going from -42 2.65 mv to -40 1.87 mv. A one-way ANOVA test revealed these small changes to be unimportant ( $P > 0.05$ ).

According to earlier theories,<sup>52</sup> the high rigidity of the lipid membrane of the nanovesicles and their capacity to hold the medication may be the causes of the optimized formula's physical stability.

### Evaluation of Optimized Hyaluronated CIT-HA\*TBLs Thermogel

Incorporating the CIT-HA\*TBLs formula with the poloxamer 407, poloxamer 188, and CAP971 polymers results in the proper viscosity and bioadhesive properties.<sup>123</sup> The hyaluronated CIT-HA\*TBLs formula and the thermogel bases were successfully combined. At body temperature and room temperature, the viscosities of the CIT-HA\*TBLs thermogel were  $8604.96 \pm 43.4$  and  $648.37 \pm 35.7$  cp, respectively. Good pseudo-plasticity and thixotropic behavior were confirmed by rheological parameters with Farrow's constant (N) values higher than 1.

The hysteresis loop area gave values of 2446.7 and 1839.4 dyne/cm<sup>2</sup>. sec for the thermogel at room and body temperatures, respectively. Comparing the release and ex vivo permeation patterns of the CIT-HA\*TBLs thermogel to the Control thermogel is shown in Figure 6A and B. The findings demonstrate that the CIT-HA\*TBLs thermogel performed better than the control CIT thermogel in terms of low release and high Q<sub>24</sub>. Citicoline was released from the CIT-HA\*TBLs thermogel formula at a rate of 63.82.75%, compared to 77.571.62% for control thermogel over an 8-hour period. This is illustrated by the fact that the TBLs nanovesicles capture the CIT medication, which prolongs and sustains the CIT release compared to the un entrapped drug. Additionally, the CIT-HA\*TBLs showed significantly more drug permeation than the control thermogel after 24 hours  $443.1 \pm 3.3$  μg/cm<sup>2</sup>.

The CIT-TBLs \*HA thermogel's gelation temperature provided a good value of 33.095 that is thought to be suitable for nasal application. This degree causes it to be in a fluid state at room temperature, making administration simpler and dosage calculations more accurate. It also causes it to become an adhesive gel with increasing residence duration near the lower limit of the nasal physiological temperature range (32–37c).

## In vivo Study

### Effect of Treatments on Hippocampal Levels of NFκB and MDA in Rats of AIC13-Induced AD

The mean value results of rats subjected to AIC13 significantly raised hippocampal tissue homogenate levels of NFκB and MDA to  $6.83 \pm 0.37$  and  $5.07 \pm 0.10$  by 421.60% and 603.57%, respectively, as compared to the normal control group  $1.62 \pm 0.12$  and  $0.84 \pm 0.02$ . On the other hand, treatment with CIT solution, Control thermogel, CIT-TBLs thermogel, CIT-HA\*TBLs thermogel, and HA\*TBLs thermogel via an intranasal application for consecutive 2 weeks restoring both NFκB  $6.06 \pm 0.08$ ,  $5.08 \pm 0.05$ ,  $4.42 \pm 0.27$ ,  $2.00 \pm 0.00$  and  $4.38 \pm 0.33$ , respectively, by 88.73%, 74.48%, 64.72%,

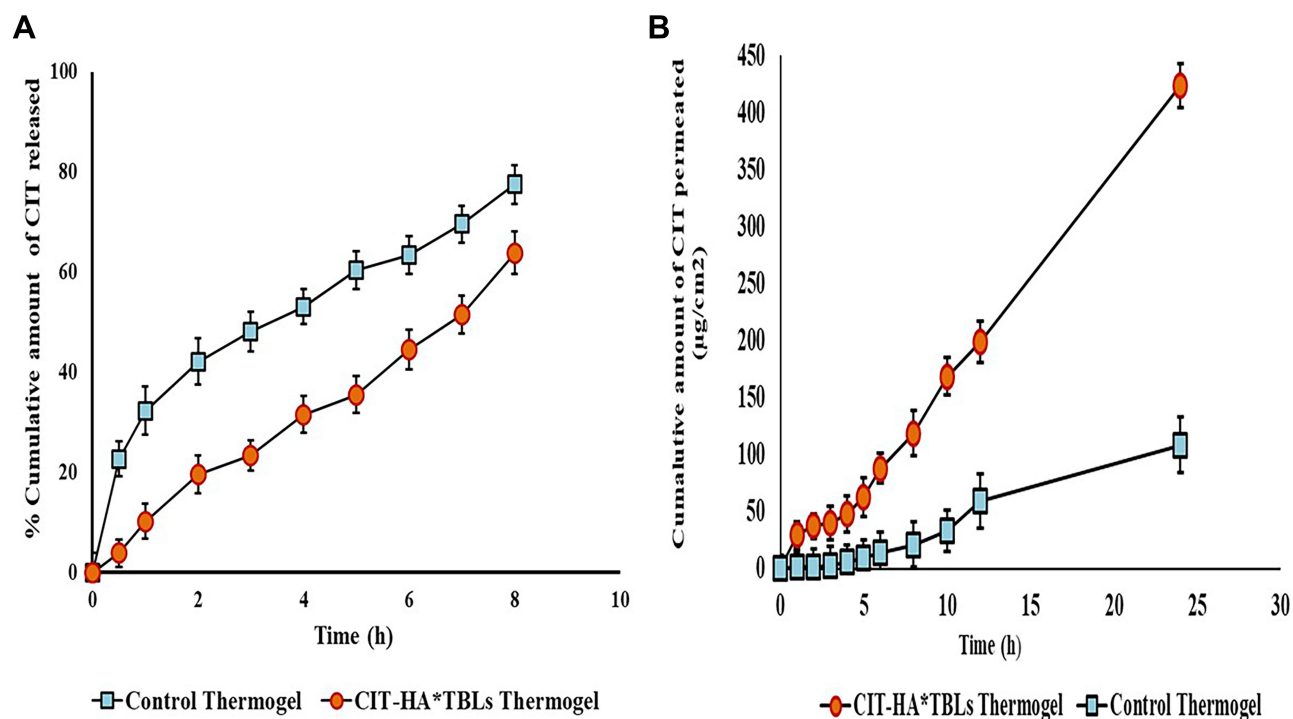


**Figure 6** Dissolution profiles (a) and permeation profiles (b) of CIT from the control thermogel and CIT-HA\*TBLs thermogel.

29.28%, and 64.13% as compared to positive control rats. Additionally, MDA mean results represent significant decrease when compared to positive control group to  $4.13 \pm 0.12$ ,  $3.66 \pm 0.08$ ,  $2.95 \pm 0.10$ ,  $0.99 \pm 0.01$ , and  $3.20 \pm 0.05$  by about 81.48%, 72.29%, 58.18%, 19.53 and 63.12%, respectively. The intranasal applied CIT-HA\*TBLs thermogel restored both NF $\kappa$ B and MDA to normal levels (Table 5). Our observed effect represents CIT-HA\*TBLs thermogel protecting animals from aluminum chloride-induced neurodegenerative damage. Previous data represent that AlCl<sub>3</sub>-induced memory impairment is thought to be caused by a variety of ways<sup>124</sup> AlCl<sub>3</sub> cognitive toxicities have been linked to the upregulation of APP, Ab, NF- $\kappa$ B, AChE activity, nitric oxide release, oxidative stress, and the eventual neuronal apoptosis.<sup>125,126</sup>

**Table 5** Presentation of Cerebral Cortex Hemisphere Tissue NF $\kappa$ B and MDA Concerning the Effect of 2 Weeks (0.9mg/kg) Intranasal Administration of Treatment in Different Experimental Groups

Groups	NF $\kappa$ B (ng/mg)	MDA (n.mol/mg)
Normal control	$1.62 \pm 0.12$	$0.84 \pm 0.02$
Positive control	$6.83 \pm 0.37^a$	$5.07 \pm 0.10^a$
CIT solution	$6.06 \pm 0.08^{b,f}$	$4.13 \pm 0.12^{a,b,e,f,g}$
Control thermogel	$5.08 \pm 0.05^{a,b,f}$	$3.66 \pm 0.08^{a,d,e,f}$
CIT-TBLs thermogel	$4.42 \pm 0.27^{a,b,f}$	$2.95 \pm 0.10^{a,b,d,c,e,f}$
CIT-HA*TBLs thermogel	$2.00 \pm 0.00^{a,c,d,e,g}$	$0.99 \pm 0.01^{b,d,c,e,f,g}$
HA*TBLs thermogel	$4.38 \pm 0.33^{a,b,f}$	$3.20 \pm 0.05^{b,d,g}$

**Notes:** AD: Alzheimer's the mean of 6–8 values  $\pm$  standard error of the mean (S.E.M). <sup>a</sup>Significantly different from the normal control group, <sup>b</sup>Significantly different from the positive control group, <sup>c</sup>CIT solution group; <sup>d</sup>Control thermogel; <sup>e</sup>CIT-TBLs thermogel; <sup>f</sup>CIT-HA\*TBLs thermo gel; <sup>g</sup>HA\*TBLs thermogel group at  $p < 0.05$ .

Furthermore, Abdel-Zaher et al<sup>127</sup> indicated aluminum poisoning damages cytoplasmic membranes and disrupts neuronal integrity, whereas citicoline protects neurons from this damage and improves memory. Consequently, D-galactose-induced subacute aging models reveal memory loss and neuroinflammation linked to NFκB activation/reticuloendotheliosis viral oncogene homolog A (RelA) activation and decreased sirtuin 1 (SIRT1) expression in the hippocampus. Salidroside reduces memory impairments and inflammatory mediators, including TNF- and IL-1 in D-gal-treated animals. SIRT1 is up-regulated by salidroside, inhibiting the NFκB pathway.<sup>128,129</sup> Otherwise, the lipopolysaccharide mice sepsis model reported that the NFκB transcription factor regulates the generation of pro-inflammatory factors via the phosphatidylinositol-3-kinase/protein kinase B (PI3K/Akt) signaling pathway.<sup>130</sup>

In addition, the streptozotocin-induced neurodegenerative disorder mice model indicates that liposomal citicoline therapy increases pro-inflammatory cytokines NF-κB, TNF-, IL-6, IL-8, and MCP-1.<sup>131,132</sup> All these data confirmed our results that intranasal citicoline significantly reduces NFκB hippocampus tissue levels (Table 5). In this study, the administration of AlCl<sub>3</sub> resulted in learning and memory impairments, and an increase followed this in oxidative stress levels; an increase in hippocampus MDA levels. According to several previous studies, aluminum chloride can cause a cytotoxic effect via the induction of oxidative stress.<sup>133</sup> Indeed, the AlCl<sub>3</sub>-induced parkinsonism model depended on apoptosis, and oxidative stress biomarkers increased, especially MDA and Catalase (CAT).<sup>134</sup> Also, according to Henderson et al.<sup>135</sup> Reactive oxygen species (ROS) production causes neuronal cell death and apoptosis via Bax expression and mitochondrial translocation.

Furthermore, the glial fibrillary acidic protein (GFAP) upregulation in astrocytes has been linked to Aβ<sub>1-42</sub> and oxidative stress produced by amyloidogenic-hyperlipidemic and other pathogenic processes of AD.<sup>136</sup> Additionally, oxidative stress activates nicotinic amide adenine dinucleotide phosphate (NADPH) oxidase, which induces the production of neuroinflammatory markers, including tumor necrosis factor-α TNF-α and NFκB, which contribute to AD development.<sup>137,138</sup> In addition to amyloid plaque buildup, AD transgenic animal's exhibit oxidative brain injury.<sup>139</sup> Consequently, stress-activated protein kinases, including c-Jun N-terminal kinases (JNK), p38 mitogen-activated protein kinases (MAPKs), and extracellular-signal-regulated kinases 1/2 (ERK1/2), and changes in redox-sensitive transcription factors may have a role in Alzheimer's disease pathogenesis, according to the findings of these studies.<sup>140-142</sup> Most previous studies on oxidative damage in AD have explained why the AD brain produces more ROS.<sup>143</sup> Mitochondrial malfunction due to oxidative stress may also play a role in developing ROS, particularly with the metal liganded with Aβ.<sup>144</sup>

In agreement with Al-Kuraishy et al,<sup>145</sup> citicoline increased psychomotor vigilance, arousal, and visual working memory while reducing oxidative stress in healthy participants. Also, the research found that giving adolescent males CIT for consecutive 28 days improved psychomotor function, cognitive-attention activity, and reduced impulsivity.<sup>146</sup> Recently, neuroprotection has been focusing on the role of inflammation and oxidative stress.<sup>147</sup>

Furthermore, citicoline has been shown to protect against neurodegenerative disorders in animal and human trials.<sup>148</sup> All these data agree with our results that the intranasal CIT has been modulating MDA brain tissue levels (Table 5).

### Effect of Treatments on Hippocampal miRNA 137-Gene Expression in Rats of AlCl<sub>3</sub>-Induced AD

The miRNA-137 regulates glutamatergic synaptic transmission and plasticity in the hippocampus by modulating genes' translation at different ends of the synapse. The current functional miRNA-137 data support the idea that miRNAs can modulate complex gene regulation networks implicated in common physiological pathways. From this point of view, our mean value data represent that miRNA 137 genetic expression significantly increased via aluminum chloride exposure to  $7.01 \pm 1.32$  by 701% compared to the normal control rat's mean of  $1.00 \pm 0.01$ .

In contrast, treatment with CIT Solution, Control thermogel, CIT-BLs thermogel, CIT-HA\*TBLs thermogel, and HA\*TBLs thermogel via an intranasal application for consecutive 2 weeks represent a significant decrease in miRNA 137 mean gene expression values to  $5.09 \pm 0.53$ ,  $4.19 \pm 0.14$ ,  $3.43 \pm 0.52$ ,  $1.76 \pm 0.21$  and  $3.88 \pm 0.31$ , respectively. The CIT-HA\*TBLs thermogel restoring miRNA 137 mean genetic expression back to normal compared to the positive control group and the normal one (Figure 7). All recent studies have shown that miRNA is involved in neurodegenerative disorder, although the initial patient investigations on synapse represent elevated miRNA-137 levels.<sup>149</sup> Early glutamatergic synaptic formation and aberrant glutamatergic synaptic maturation have recently been established either in AD or

## miRNA 137 Gene expression

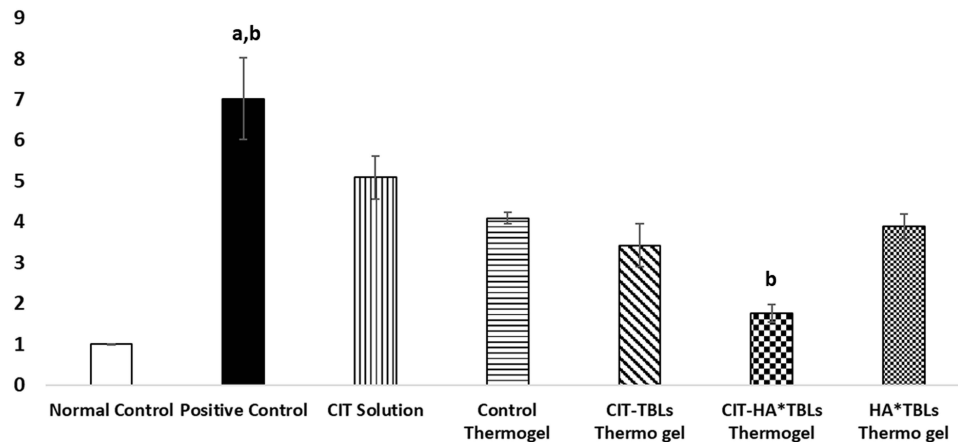


**Figure 7** Bar chart presentation of hippocampal tissue miRNA 137 gene expression levels concerning the effect of 2 weeks (0.9mg/kg) intranasal administration of CIT Solution, Control thermo gel, CIT-TBLs thermo gel, CIT-HA\*TBLs thermo gel, and HA\*TBLs thermo gel against  $AlCl_3$ -induced AD disease. AD: Alzheimer's disease. The mean of 6–8 values  $\pm$  standard error of the mean (S.E.M). <sup>a</sup>Significantly different from the normal control group, <sup>b</sup>Significantly different from the positive control group, at  $p < 0.05$ .

schizophrenia patients. Both are likely results of lost miRNA-137 function during brain development in severe cognitive impairments.<sup>150,151</sup>

Additionally, the postmortem prefrontal cortex tissue revealed that single nucleotide polymorphism homozygote was related to reduced miRNA-137 expression, which may induce bipolar or schizophrenia<sup>152,153</sup> Moreover, a kainic acid promotes hippocampus seizures convulsion in mice, indicating that Interhippocampal injection of anti-microRNA oligonucleotides targeting microRNA-124 and -137 normalized neuroblast proliferation and prevented memory loss and nerve damage<sup>154</sup> Furthermore, the latest research suggests that miRNA-137 may have a role in drug addiction inpatient for methamphetamine cessation<sup>155</sup> although its exact involvement remains uncertain.

The microRNA-137 affects neuronal growth and synaptic plasticity.<sup>156</sup> Recently, in an in vitro Alzheimer's disease model, the SNHG19/hsa-miRNA-137 epigenetic axis regulates  $A\beta$  25–35-induced human neuroblastoma cell line (SH-SY5Y) cytotoxicity.<sup>157</sup> Otherwise, the prostate cancer experimental model indicates that deregulation of microRNA significantly regulates MDA levels and inhibits cell proliferation, metastasis, and apoptosis.<sup>158</sup> The modulation of microRNA circulating levels has also been shown to regulate ROS levels and trigger cell autophagy in a breast cancer model, which is beneficial to patient therapy<sup>159</sup> Additionally, the Kruppel-like factor 15 (KLF15) is downregulated by miRNA-137-3p overexpression in an ischemia/reperfusion-induced cardiomyocyte animal model study.<sup>160</sup> Indeed, all recent studies confirmed our data results from miRNA-137-3p downregulation's critical role in cell survival, preventing cell apoptosis and neural damage.

### Histopathological Study

The microscopic examination of brain sections from the normal group revealed normal cerebral cortex and different hippocampus regions. On the contrary, the positive control group showed diffuse gliosis with thickened and congested blood vessels in the cerebral cortex. Numerous dark degenerating neurons were detected. Group 3 received CIT-Solution and showed the variable number of dark degenerated neurons in the cerebral cortex associated with mild-to-moderate vascular thickening, fewer degenerated neurons were detected in the CA-2 and CA-4 regions of the hippocampus. Brain sections from Group 4 received Control thermo gel showed degenerating neurons in the cerebral cortex with neuronophagia either some of the examined sections showed proliferating cerebral vasculature coupled with hippocampus exhibited few degenerating neurons in its different regions.

In contrast, Group 5 received CIT-TBLs thermo gel normal cerebral cortex examination coupled with a hippocampus few dark degenerating neurons scattered in the different regions. Concerning the brain section from Group 6 CIT-HA\*TBLs thermo gel represent cerebral cortex and hippocampus regions of the examined brain sections were apparently

regular. While Group 7 received HA\*TBLS thermogel showed apparently normal cerebral cortex in some of the examined sections with neuronal degeneration and neuronophagia in some other sections. Hippocampus showed variable number of shrunk degenerating neurons scattered in different regions (Figure 8).

Additionally, the severity of histopathological alterations in different experimental group's brain regions, cerebral cortex, and hippocampus was evaluated by assigning semi-quantitative score quantitative analysis, with a score of –

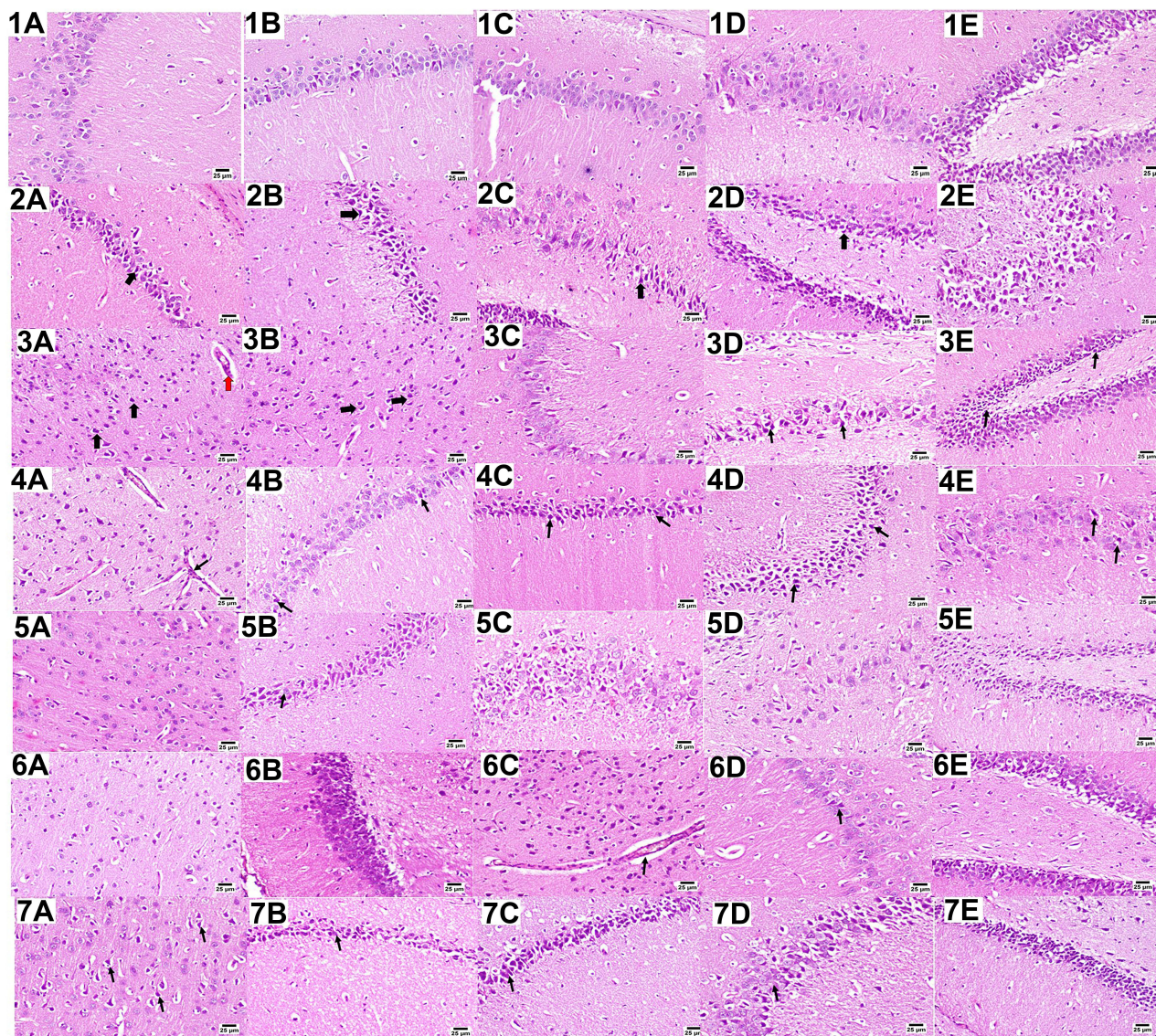


**Figure 8** Microscopic photomicrograph brain H&E staining with a higher magnification represents; (1A–1E) Normal control sections (25 µm) showing the normal histological structure of cornu ammonis hippocampus pyramidal neurons (CA-1- CA-2, CA-3, CA-4) and dentate gyrus (DG); (2A–2E) Positive control group showing numerous dark degenerated neurons in CA-1- CA-2, CA-3, CA-4 and DG regions (black arrow); Group 3 received CIT drug solution (3A) showing some degenerating neurons in the cerebral cortex (black arrows) with mild vascular thickening (red arrow), (3B and 3C) sections showing few degenerating neurons (black arrows) in CA-1, CA-2, CA-3, (3D) sections showing few degenerating neurons CA-4; (3E) showing some degenerating neurons with DG region of hippocampus; sections from Group 4 received Control thermogel (4A) showing neuronal degeneration and neuronophagia (black arrows) in cerebral cortex with congested blood vessels, (4B–4D) showing some degenerating neurons (black arrows) in CA-1 CA-2, CA-3, CA-4 region of hippocampus and 4E: showing some degenerating neurons in DG region of hippocampus; Group 5 received CIT-TBLS thermogel 5A: showing apparently normal cerebral cortex, (5B and 5C) showing few degenerating neurons in CA-1, CA-2, and CA-3 region of hippocampus while (5D) showing CA-4 hippocampus region apparently normal structure and (5E) showing few degenerating neurons in DG region of hippocampus; Group 6 received CIT-HA\*TBLS thermogel (6A) showing apparently normal cerebral cortex, (6B) showed average normal hippocampus and (6C) represent a normal cerebral cortex and (6D) showing apparently normal CA1 region of hippocampus (black arrows) normal histological structure of DG regions; Group 7 receiving HA\*TBLS thermogel (7A) showing few neuronal degenerations with neuronophagia (black arrows) in the cerebral cortex; (7B–7D) showing number of degenerating neurons in the CA-1, CA-2, and CA-3 region of hippocampus (black arrows) and CA4 showing number of degenerating neurons in the region of hippocampus with marked cellular loss (black arrows); (7E) showing number of degenerating neurons in the DG region of hippocampus.

assigned the absence of any detectable lesions in normal brain sections, + sections with mild histopathological changes, ++ assigned to the sections that represent moderate histopathological changes, while a severe represented lesion was assigned with +++ label CIT-TBLs thermogel, CIT-HA\*TBLs thermogel, and HA\*TBLs thermogel sections showed significantly lower scoring compared with positive control AD sections with restoring vascular brain integrity to normal (Table 6). Almuhayawi et al,<sup>160</sup>

Alzheimer's rat model represents induction of AD-induced unorganized cerebral cortex with shrinkage neuron treated. Citicoline's crucial significance in reestablishing normal brain and cerebral cortex structure is also demonstrated by tramadol-induced neurodegenerative diseases.<sup>161</sup> Furthermore, the epilepsy rat model treated via the citicoline intranasal route potentially enhances neurons.<sup>162</sup> These data supported our histopathological examination of the brain and hippocampus region (Figure 8).

### Immunohistochemistry Assay

Negative immune staining for A $\beta$ <sub>1-42</sub> was detected in both the cerebral cortex and hippocampus of the normal control group. On the contrary, the positive control group showed increased immune reactivity expression of A $\beta$ <sub>1-42</sub> in both the cerebral cortex and hippocampus that increased to about 42.1-fold compared to the Normal group. Brain sections of Group 3 received CIT solution revealed moderate positive immune staining expression for A $\beta$ <sub>1-42</sub> decreased to about 18.3-fold compared to positive control group. Likewise, Group 4 received Control thermogel exhibited moderate amounts of A $\beta$ <sub>1-42</sub> immune staining expression in the examined brain sections to about 20.2-fold compared to the positive control group. Group 5 received CIT-TBLs thermogel all examined brain sections noticed a minimal negative A $\beta$ <sub>1-42</sub> immune staining that decreased to about 31.1-fold compared to the positive control group.

Additionally, negative expression of A $\beta$ <sub>1-42</sub> detected in all examined sections of Group 6 received CIT-HA\*TBLs thermogel that decreased to about 60.9-fold and minimal A $\beta$ <sub>1-42</sub> expression for Group 7 received HA\*BL thermogel decreased to about 46.8-fold compared to the positive control group (Figure 9A and B). Our results indicated that the application of intranasal CIT-HA\*TBLs thermogel for 2 weeks restored brain and extracellular matrix structure via suppressing A $\beta$ <sub>1-42</sub> expression.

In agreement with our results, a high-fat diet/overectomy/D-galactosamine-induced Alzheimer's disease rat model confirmed the elevation of A $\beta$ <sub>1-42</sub> expression in the diseased animal that was down-regulated by perindopril treatment in the brain hippocampus.<sup>163</sup> Also, many researchers enrolled that the imbalance of homeostasis for Ach resulted in the deposition of A $\beta$ -induced neural damage; indeed, the drug treatment enhancing Ach levels promotes A $\beta$  degradation restoring neural damage caused via Alzheimer's disease induction.<sup>164-166</sup>

## Conclusions

In the current study, a brand-new nano platform carrier (TBLs) for the intranasal administration of CIT for the treatment of AD was created. TBLs were created using the method of thin-film hydration and were appropriately optimized using the Box-Behnken design. The improved TBLs composition, which included 300 mg of PL 90 G, 43.97 mg of SP 60, and 20 mg of SDC, was decorated on the surface with HA. The high EE percentage of 74±45, sustained-release Q8h of 81.27±5.4%, high permeation Q24h of 512.43±19.58  $\mu$ g/cm<sup>2</sup>, minor VS (178±8.92 nm), and high ZP (42±3.6 mV) were assessed for the CIT-HA\*TBLs formula. The CIT-HA\*TBLs thermogel was also able to

**Table 6** Histopathological Lesion Score in Cerebral Cortex and Hippocampus Regions in Different Experimental Groups

Lesions	Groups						
	Normal Control	Positive Control	CIT Solution	Control Thermogel	CIT-TBLs Thermogel	CIT-HA*TBLs Thermogel	HA*TBLs Thermogel
Neuronal degeneration	–	+++	++	++	+	–	+
Vascular changes	–	+++	++	++	–	–	–
Gliosis	–	+++	++	+	+	–	+

**Notes:** +++ Severe histopathological changes; ++ Moderate histopathological changes; + Mild histopathological changes; – Absence of any detectable lesions.

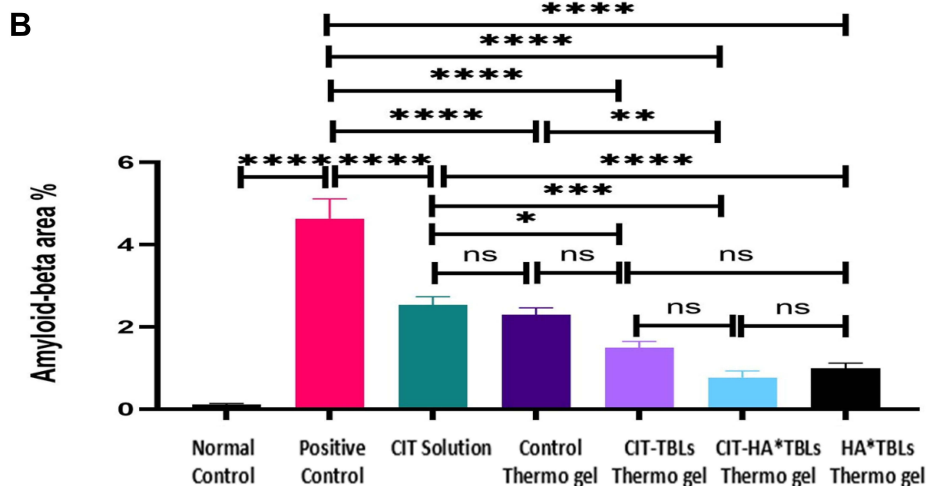
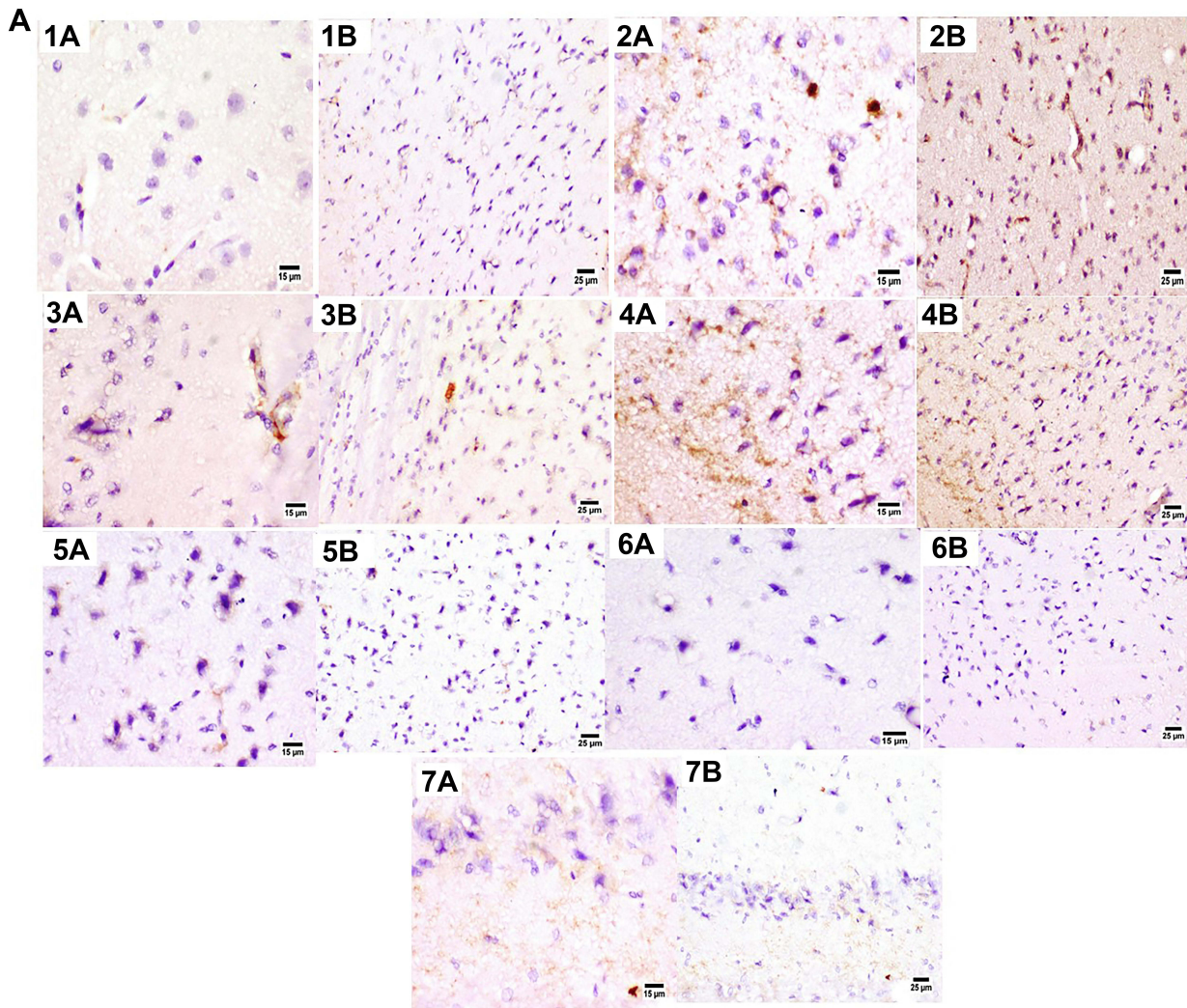


**Figure 9 (A)** Photomicrograph of brain  $A\beta_{1-42}$  immune staining showing at higher magnification 15  $\mu m$  and 25  $\mu m$  for Group 1 normal control group negative reactivity to  $A\beta_{1-42}$  staining (Figure 1A and B); The positive control group showing strong reactivity for  $A\beta_{1-42}$  staining (Figure 2A and B); Group 3 received CIT solution, and Group 4 received control thermogel showing moderate reactivity for  $A\beta_{1-42}$  staining (Figures 3A, 3B; 4A and 4B); also Group 5 received CIT-TBLs thermogel represents a minimal negative reactivity toward  $A\beta_{1-42}$  staining (Figure 5A and B); Group 6 CIT-HA\*TBLS thermogel showing negative reactivity toward  $A\beta_{1-42}$  staining (Figure 6A and B); Group 7 received HA\*TBLS thermogel showing minimal positive reactivity staining for  $A\beta_{1-42}$  staining (Figure 7A and B). **(B)** Statistical analysis of  $A\beta$  area expression was conducted in different experimental groups. Data is presented as means  $\pm$ SE, significance was considered at  $P < 0.05$ . \*Significantly different from control at  $P < 0.05$ , \*\* Significantly different from positive control at  $P < 0.05$ , \*\*\*Significantly different from CIT solution at  $P < 0.05$ . \*\*\*\*Significantly different from CIT solution at  $P < 0.05$ . ns No Significantly different from presented at  $P < 0.05$ .

overcome the two main barriers to CIT's passage through the BBB, which are its high hydrophilicity and rapid metabolism. The CIT was professionally and quickly delivered to the brain via the intranasal route owing to the designed CIT-HA\*TBLs thermogel. The CIT-HA\*TBLs thermogel significantly outperformed in pharmacodynamic tests than the CIT-TBLs thermogel, CIT-thermogel, HA-TBLs thermogel, and CIT solution. According to the in vivo findings, we came to the conclusion that CIT-HA\*TBLs formula might be promising agents for treating neurodegenerative disorder by reversing hippocampus neurodegenerative injury by boosting cholinergic activity through down-regulation of hippocampus miR-137 and  $\text{A}\beta_{1-42}$  expression in conjunction with a reduction in oxidative stress biomarker release MDA and inflammatory NF- $\kappa$ B biomarkers. The CIT-HA\*TBLs thermogel offers a potential formula for restoring the integrity of the hippocampus during neurodegenerative disorders, which permits it to be employed as a neuroprotective and anti-Alzheimer's drug. This is strongly supported by the results of this research.

## Acknowledgments

We appreciate D Yasmin M Ahmed's help with the pharmacological investigations at Nahda University's Faculty of Pharmacy and Department of Pharmacology. The South Valley University and researchers are working to get the current patent authorized by the Egyptian Patent Office in the name of (Citi-Hyalurosomes Intranasal Thermogel) with application number of EG/PL2022/1529.

## Disclosure

The authors report no other potential conflicts of interest in relation to this work and affirm that they have no financial conflicts of interest and that neither the study nor the creation of this manuscript received any support.

## References

1. Goedert M, Spillantini MG. A century of Alzheimer's disease. *Science*. 2006;314(5800):777–781. doi:10.1126/science.1132814
2. Fortea J, Vilaplana E, Carmona-Iragui M, et al. Clinical and biomarker changes of Alzheimer's disease in adults with Down syndrome: a cross-sectional study. *Lancet*. 2020;395(10242):1988–1997. doi:10.1016/S0140-6736(20)30689-9
3. Van Zeller M, Dias D, Sebastião AM, et al. NLRP3 inflammasome: a starring role in amyloid- $\beta$ - and tau-driven pathological events in Alzheimer's disease. *J Alzheimers Dis*. 2021;83(3):939–961. doi:10.3233/JAD-210268
4. Cassidy L, Fernandez F, Johnson JB, et al. Oxidative stress in Alzheimer's disease: a review on emergent natural polyphenolic therapeutics. *Complement Ther Med*. 2020;49:102294. doi:10.1016/j.ctim.2019.102294
5. Jahn H. Memory loss in Alzheimer's disease. *Dialogues Clin Neurosci*. 2022;15. doi:10.31887/DCNS.2013.15.4/hjahn
6. Siddiqui A, Shah Z, Jahan RN, et al. Mechanistic role of boswellic acids in Alzheimer's disease: emphasis on anti-inflammatory properties. *Int J Cancer*. 2021;144:112250. doi:10.1016/j.biopha.2021.112250
7. Wilson ES, Litwa K. Synaptic hyaluronan synthesis and CD44-mediated signaling coordinate neural circuit development. *Cells*. 2021;10(10):2574. doi:10.3390/cells10102574
8. Geissler M, Gottschling C, Aguado A, et al. Primary hippocampal neurons, which lack four crucial extracellular matrix molecules, display abnormalities of synaptic structure and function and severe deficits in perineuronal net formation. *J Neurosci*. 2013;33(18):7742–7755. doi:10.1523/JNEUROSCI.3275-12.2013
9. Jimenez-Vergara AC, Van Druenen R, Cagle T, et al. Modeling the effects of hyaluronic acid degradation on the regulation of human astrocyte phenotype using multicomponent interpenetrating polymer networks (mIPNs). *Sci Rep*. 2020;10(1):1–14. doi:10.1038/s41598-020-77655-1
10. Misra S, Hascall VC, Markwald RR, et al. Interactions between hyaluronan and its receptors (CD44, RHAMM) regulate the activities of inflammation and cancer. *Front Immunol*. 2015;6:201. doi:10.3389/fimmu.2015.00201
11. Sun Y, Xu S, Jiang M, et al. Role of the extracellular matrix in Alzheimer's disease. *Front Aging Neurosci*. 2021;13:707466. doi:10.3389/fnagi.2021.707466
12. Wenk GL. Neuropathologic changes in Alzheimer's disease. *Biochem J*. 2003;364:7–10.
13. Bekdash RA. The cholinergic system, the adrenergic system and the neuropathology of Alzheimer's disease. *Int J Mol Sci*. 2021;22(3):1273. doi:10.3390/ijms22031273
14. Liu PP, Xie Y, Meng XY, et al. History and progress of hypotheses and clinical trials for Alzheimer's disease. *Signal Transduct Target Ther*. 2019;4(1):1–22. doi:10.1038/s41392-018-0034-5
15. Maciejewska K, Czarnecka K, Szymański P. A review of the mechanisms underlying selected comorbidities in Alzheimer's disease. *Pharmacol Rep*. 2021;73(6):1565–1581. doi:10.1007/s43440-021-00293-5
16. Adibhatla RM, Hatcher J. Cytidine 5'-diphosphocholine (CDP-choline) in stroke and other CNS disorders. *Neurochem Res*. 2005;30(1):15–23. doi:10.1007/s11064-004-9681-8
17. Castagna A, Cotroneo AM, Ruotolo G, et al. The CITIRIVAD study: cITicoline plus RIVastigmine in elderly patients affected with dementia study. *Clin Drug Investig*. 2016;36(12):1059–1065. doi:10.1007/s40261-016-0454-3
18. Grieb P. Neuroprotective properties of citicoline: facts, doubts and unresolved issues. *CNS Drugs*. 2014;28(3):185–193. doi:10.1007/s40263-014-0144-8

19. Adibhatla RM, Hatcher JF, Tureyan K. CDP-choline liposomes provide significant reduction in infarction over free CDP-choline in stroke. *Brain Res.* 2005;1058(1–2):193–197. doi:10.1016/j.brainres.2005.07.067
20. Pradhan D, Tambe V, Raval N, et al. Dendrimer grafted albumin nanoparticles for the treatment of post cerebral stroke damages: a proof of concept study. *Colloids Surf B Biointerfaces.* 2019;184:110488. doi:10.1016/j.colsurfb.2019.110488
21. Trucillo P, Campardelli R, Reverchon E. Liposomes: from bangham to supercritical fluids. *Processes.* 2020;8(9):1022. doi:10.3390/pr8091022
22. Liu W, Hou Y, Jin Y, et al. Research progress on liposomes: application in food, digestion behavior and absorption mechanism. *Trends Food Sci Technol.* 2020;104:177–189. doi:10.1016/j.tifs.2020.08.012
23. Hua S. Lipid-based nano-delivery systems for skin delivery of drugs and bioactives. *Front Pharmacol.* 2015;6:219. doi:10.3389/fphar.2015.00219
24. Sercombe L, Veerati T, Moheimani F, et al. Advances and challenges of liposome assisted drug delivery. *Front Pharmacol.* 2015;6:286. doi:10.3389/fphar.2015.00286
25. Lombardo D, Calandra P, Barreca D, et al. Soft interaction in liposome nanocarriers for therapeutic drug delivery. *Nanomaterials.* 2016;6(7):125. doi:10.3390/nano6070125
26. Liu W, Ye A, Han F, et al. Advances and challenges in liposome digestion: surface interaction, biological fate, and GIT modeling. *Adv Colloid Interface Sci.* 2019;263:52–67. doi:10.1016/j.cis.2018.11.007
27. Zylberberg C, Matosevic S. Pharmaceutical liposomal drug delivery: a review of new delivery systems and a look at the regulatory landscape. *Drug Deliv.* 2016;23(9):3319–3329. doi:10.1080/10717544.2016.1177136
28. Olusanya TO, Haj Ahmad RR, Ibegbu DM, et al. Liposomal drug delivery systems and anticancer drugs. *Molecules.* 2018;23(4):907. doi:10.3390/molecules23040907
29. Cevc G, Blume G. Lipid vesicles penetrate into intact skin owing to the transdermal osmotic gradients and hydration force. *Biochim Biophys Acta Biomembr.* 1992;1104(1):226–232. doi:10.1016/0005-2736(92)90154-E
30. Kumar KKPS, Kumar RSR. Review on transferosomes and transferosomal gels. *J Pharm Res Int.* 2021;33:114–126. doi:10.9734/jpri/2021/v33i43B32532
31. Solanki D, Kushwah L, Motiwale M, et al. Transferosomes-a review. *World J Pharm Pharmaceut Sci.* 2016;5(10):435–449 doi:10.20959/wjpps201610-7845.
32. Stojančević M, Pavlović N, Goločorbin-Kon S, et al. Application of bile acids in drug formulation and delivery. *Front Life Sci.* 2013;7(3–4):112–122. doi:10.1080/21553769.2013.879925
33. Rajput T, Chauhan MK. Bilosome: a bile salt based novel carrier system gaining interest in pharmaceutical research. *J Drug Deliv Therapeut.* 2017;7(5):4–16. doi:10.22270/jddt.v7i5.1479
34. Mohsen AM, Salama A, Kassem AA. Development of Acetazolamide loaded bilosomes for improved ocular delivery: preparation, characterization and in vivo evaluation. *J Drug Deliv Sci Technol.* 2020;59:101910. doi:10.1016/j.jddst.2020.101910
35. Shukla A, Khatri K, Gupta PN, et al. Oral immunization against hepatitis B using bile salt stabilized vesicles (bilosomes). *J Pharm Pharmaceut Sci.* 2008;11(1):59–66. doi:10.18433/J3K01M
36. El Menshawe SF, Aboud HM, Elkomy MH, et al. A novel nanogel loaded with chitosan decorated bilosomes for transdermal delivery of terbutaline sulfate: artificial neural network optimization, in vitro characterization and in vivo evaluation. *Drug Deliv Transl Res.* 2020;10(2):471–485. doi:10.1007/s13346-019-00688-1
37. Mosallam S, Sheta NM, Elshafeey AH, et al. Fabrication of highly deformable bilosomes for enhancing the topical delivery of terconazole: in vitro characterization, microbiological evaluation, and in vivo skin deposition study. *AAPS PharmSciTech.* 2021;22(2):1–12. doi:10.1208/s12249-021-01924-z
38. Nasr M. Development of an optimized hyaluronic acid-based lipidic nanoemulsion co-encapsulating two polyphenols for nose to brain delivery. *Drug Deliv.* 2021;23(4):1444–1452. doi:10.3109/10717544.2015.1092619
39. Erdő F, Bors LA, Farkas D, et al. Evaluation of intranasal delivery route of drug administration for brain targeting. *Brain Res Bull.* 2018;143:155–170. doi:10.1016/j.brainresbull.2018.10.009
40. Yang H, Liu Z, Song Y, et al. Hyaluronic acid-functionalized bilosomes for targeted delivery of tripterine to inflamed area with enhance therapy on arthritis. *Drug Deliv.* 2019;26(1):820–830. doi:10.1080/10717544.2019.1636423
41. Conacher M, Alexander J, Brewer JM. Oral immunisation with peptide and protein antigens by formulation in lipid vesicles incorporating bile salts (bilosomes). *Vaccine.* 2001;19(20–22):2965–2974. doi:10.1016/S0264-410X(00)00537-5
42. Peer D, Margalit R. Loading mitomycin C inside long circulating hyaluronan targeted nano-liposomes increases its antitumor activity in three mice tumor models. *Int J Cancer.* 2004;108(5):780–789. doi:10.1002/ijc.11615
43. Bangham AD, Standish MM, Watkins JC. Diffusion of univalent ions across the lamellae of swollen phospholipids. *J Mol Biol.* 1965;13(1):238–IN27. doi:10.1016/S0022-2836(65)80093-6
44. Borumand MR. Preparation and characterization of sodium alginate nanoparticles containing ICD-85 (venom derived peptides). *Int J Res Sci Innov Appl Stud.* 2013;4(3):534–542.
45. Goindi S, Kumar G, Kumar N, et al. Development of novel elastic vesicle-based topical formulation of cetirizine dihydrochloride for treatment of atopic dermatitis. *Aaps Pharmscitech.* 2013;14(4):1284–1293. doi:10.1208/s12249-013-0017-3
46. Hritcu D, Popa MI, Popa N, et al. Preparation and characterization of magnetic chitosan nanospheres. *Turk J Chem.* 2009;33(6):785–796 doi:10.3906/kim-0812-42.
47. Al-Mahallawi AM, Khawessah OM, Shoukri RA. Nano-transferosomal ciprofloxacin loaded vesicles for non-invasive trans-tympanic otological delivery: in-vitro optimization, ex-vivo permeation studies, and in-vivo assessment. *Int J Pharm.* 2014;472(1–2):304–314. doi:10.1016/j.ijpharm.2014.06.041
48. González-Rodríguez ML, Arroyo CM, Cózar-Bernal MJ, et al. Deformability properties of timolol-loaded transferosomes based on the extrusion mechanism. Statistical optimization of the process. *Drug Dev Ind Pharm.* 2016;42(10):1683–1694. doi:10.3109/03639045.2016.1165691
49. Refaat H, Naguib YW, Elsayed MM, et al. Modified spraying technique and response surface methodology for the preparation and optimization of propolis liposomes of enhanced anti-proliferative activity against human melanoma cell line A375. *Pharmaceutics.* 2019;11(11):558. doi:10.3390/pharmaceutics11110558

50. Safwat MA, Soliman GM, Sayed D, et al. Gold nanoparticles enhance 5-fluorouracil anticancer efficacy against colorectal cancer cells. *Int J Pharm.* 2016;513(1–2):648–658. doi:10.1016/j.ijpharm.2016.09.076
51. Salem HF, Kharshoum RM, Awad SM, et al. Tailoring of retinyl palmitate-based ethosomal hydrogel as a novel nanoplatform for acne vulgaris management: fabrication, optimization, and clinical evaluation employing a split-face comparative study. *Int J Nanomedicine.* 2021;16:4251. doi:10.2147/IJN.S301597
52. Salem HF, Nafady MM, Kharshoum RM, et al. Mitigation of rheumatic arthritis in a rat model via transdermal delivery of dapoxetine HCl amalgamated as a nanoplatform: in vitro and in vivo assessment. *Int J Nanomedicine.* 2020;15:1517. doi:10.2147/IJN.S238709
53. Salem HF, Kharshoum RM, Abou-Taleb HA, et al. Progesterone-loaded nanosized transthesosomes for vaginal permeation enhancement: formulation, statistical optimization, and clinical evaluation in anovulatory polycystic ovary syndrome. *J Liposome Res.* 2019;29(2):183–194. doi:10.1080/08982104.2018.1524483
54. Aboud HM, Ali AA, El-Menshaweh SF, et al. Nanotransfersomes of carvedilol for intranasal delivery: formulation, characterization and in vivo evaluation. *Drug Deliv.* 2016;23(7):2471–2481. doi:10.3109/10717544.2015.1013587
55. Higuchi T. Mechanism of sustained-action medication. Theoretical analysis of rate of release of solid drugs dispersed in solid matrices. *J Pharm Sci.* 1963;52(12):1145–1149. doi:10.1002/jps.2600521210
56. Salem HF, Ali AA, Hegazy AM, et al. Harnessing of doxylamine succinate/pyridoxine hydrochloride-dual laden bilosomes as a novel combinatorial nanoparadigm for intranasal delivery: in vitro optimization and in vivo pharmacokinetic appraisal. *J Pharm Sci.* 2022;111(3):794–809. doi:10.1016/j.xphs.2021.11.007
57. Gavini E, Rassu G, Sanna V, et al. Mucoadhesive microspheres for nasal administration of an antiemetic drug, metoclopramide: in-vitro/ex-vivo studies. *J Pharm Pharmacol.* 2005;57(3):287–294. doi:10.1211/0022357055623
58. Elsayed MM, Mostafa ME, Alaaeldin E, et al. Design and characterisation of novel Sorafenib-loaded carbon nanotubes with distinct tumour-suppressive activity in hepatocellular carcinoma. *Int J Nanomedicine.* 2019;14:8445. doi:10.2147/IJN.S223920
59. Mohamad SA, Safwat MA, Elrehany M, et al. A novel nasal co-loaded loratadine and sulphiride nanoemulsion with improved downregulation of TNF- $\alpha$ , TGF- $\beta$  and IL-1 in rabbit models of ovalbumin-induced allergic rhinitis. *Drug Deliv.* 2021;28(1):229–239. doi:10.1080/10717544.2021.1872741
60. Nasr M, Mansour S, Mortada ND, et al. Vesicular aceclofenac systems: a comparative study between liposomes and niosomes. *J Microencapsul.* 2008;25(7):499–512. doi:10.1080/02652040802055411
61. Qi H, Li L, Huang C, et al. Optimization and physicochemical characterization of thermosensitive poloxamer gel containing puerarin for ophthalmic use. *Chem Pharm Bull.* 2006;54(11):1500–1507. doi:10.1248/cpb.54.1500
62. Cafaggi S, Russo E, Caviglioli G, et al. Poloxamer 407 as a solubilising agent for tolfenamic acid and as a base for a gel formulation. *Eur J Pharmaceut Sci.* 2008;35(1–2):19–29. doi:10.1016/j.ejps.2008.05.010
63. Wissing SA, Müller RH. Solid lipid nanoparticles as carrier for sunscreens: in vitro release and in vivo skin penetration. *J Control Release.* 2002;81(3):225–233. doi:10.1016/S0168-3659(02)00056-1
64. Mansour M, Mansour S, Mortada ND, et al. Ocular poloxamer-based ciprofloxacin hydrochloride in situ forming gels. *Drug Dev Ind Pharm.* 2008;34(7):744–752. doi:10.1080/03639040801926030
65. Gabal YM, Kamel AO, Sammour OA, et al. Effect of surface charge on the brain delivery of nanostructured lipid carriers in situ gels via the nasal route. *Int J Pharm.* 2014;473(1–2):442–457. doi:10.1016/j.ijpharm.2014.07.025
66. Shata A, Elkashef W, Hamouda MA, et al. Effect of artesunate vs memantine in aluminum chloride induced model of neurotoxicity in rats. *Adv Alzheimers Dis.* 2020;9(1):1–19. doi:10.4236/aad.2020.91001
67. Thenmozhi AJ, Raja TRW, Janakiraman U, et al. Neuroprotective effect of hesperidin on aluminium chloride induced Alzheimer's disease in Wistar rats. *Neurochem Res.* 2015;40(4):767–776. doi:10.1007/s11064-015-1525-1
68. Lukas SE, Kouri EM, Rhee C, et al. Effects of short-term citicoline treatment on acute cocaine intoxication and cardiovascular effects. *Psychopharmacology.* 2001;157(2):163–167. doi:10.1007/s002130100824
69. Illum L, Farraj NF, Fisher AN, et al. Hyaluronic acid ester microspheres as a nasal delivery system for insulin. *J Control Release.* 1994;29(1–2):133–141. doi:10.1016/0168-3659(94)90129-5
70. Lukas M, Neumann ID. Nasal application of neuropeptide S reduces anxiety and prolongs memory in rats: social versus non-social effects. *Neuropharmacology.* 2012;62(1):398–405. doi:10.1016/j.neuropharm.2011.08.016
71. Dhuria SV, Hanson LR, Frey WH. Intranasal delivery to the central nervous system: mechanisms and experimental considerations. *J Pharm Sci.* 2010;99(4):1654–1673. doi:10.1002/jps.21924
72. Calcagnoli F, Kreutzmann JC, de Boer SF, et al. Acute and repeated intranasal oxytocin administration exerts anti-aggressive and pro-affiliative effects in male rats. *Psychoneuroendocrinology.* 2015;51:112–121. doi:10.1016/j.psyneuen.2014.09.019
73. Lequin RM. Enzyme immunoassay (EIA)/enzyme-linked immunosorbent assay (ELISA). *Clin Chem.* 2005;51(12):2415–2418. doi:10.1373/clinchem.2005.051532
74. Duffy SC, Venkatesan M, Chothé S, et al. Development of a multiplex real-time PCR assay for mycobacterium bovis bcg and validation in a clinical laboratory. *Microbiol Spectr.* 2021;9(2):e01098–21. doi:10.1128/Spectrum.01098-21
75. Liu WW, Meng J, Cui J, et al. Characterization and function of microRNA\* s in plants. *Front Plant Sci.* 2017;8:2200. doi:10.3389/fpls.2017.02200
76. Rozen S, Skaletsky HJ. Primer3; 1998. Available from: [https://www-genome.wi.mit.edu/genome\\_software/other/primer3.Htm](https://www-genome.wi.mit.edu/genome_software/other/primer3.Htm). Accessed November 17, 2022.
77. Bancroft JD, Gamble M. *Theory and Practice of Histological Techniques*. Elsevier health sciences; 2008.
78. Merz H, Malisius R, Mannweiler S, et al. Immuno Max. A maximized immunohistochemical method for the retrieval and enhancement of hidden antigens. Laboratory Investigation. *J Tech Methods Pathol.* 1995;73(1):149–156.
79. Hashim IIA, El-Magd NFA, El-Sheakh AR, et al. Pivotal role of Acitretin nanovesicular gel for effective treatment of psoriasis: ex vivo–in vivo evaluation study. *Int J Nanomedicine.* 2018;13:1059. doi:10.2147/IJN.S156412
80. El-Badry M, Fetih G, Fathalla D, et al. Transdermal delivery of meloxicam using niosomal hydrogels: in vitro and pharmacodynamic evaluation. *Pharm Dev Technol.* 2015;20(7):820–826. doi:10.3109/10837450.2014.926919

81. Salem HF, Kharshoum RM, Sayed OM, et al. Formulation design and optimization of novel soft glycosomes for enhanced topical delivery of celecoxib and cupferron by Box–Behnken statistical design. *Drug Dev Ind Pharm.* 2018;44(11):1871–1884. doi:10.1080/03639045.2018.1504963
82. El-Menshaweh SF, Ali AA, Halawa AA, et al. A novel transdermal nanoethosomal gel of betahistine dihydrochloride for weight gain control: in-vitro and in-vivo characterization. *Drug Des Devel Ther.* 2017;11:3377–3388. doi:10.2147/DDDT.S144652
83. Vardhan MV, Sankaraiyah G, Yohan M, et al. Optimization of Parameters in CNC milling of P20 steel using Response Surface methodology and Taguchi Method. *Mater Today.* 2017;4(8):9163–9169 doi:10.1016/j.matpr.2017.07.273.
84. El-Marakby EM, Hathout RM, Taha I, et al. A novel serum-stable liver targeted cytotoxic system using valerate-conjugated chitosan nanoparticles surface decorated with glycyrrhizin. *Int J Pharm.* 2017;525(1):123–138. doi:10.1016/j.ijpharm.2017.03.081
85. Shah N, Gohil D, Seth A. Nanostructured lipid carriers: as an efficient drug delivery carrier. *Glob J Nanomed.* 2017. doi:10.19080/GJN.2017.03.555614
86. Ahmed TA. Preparation of transfersomes encapsulating sildenafil aimed for transdermal drug delivery: Plackett–Burman design and characterization. *J Liposome Res.* 2015;25(1):1–10. doi:10.3109/08982104.2014.950276
87. Avadhani KS, Manikkath J, Tiwari M, et al. Skin delivery of epigallocatechin-3-gallate (EGCG) and hyaluronic acid loaded nano-transfersomes for antioxidant and anti-aging effects in UV radiation induced skin damage. *Drug Deliv.* 2017;24(1):61–74. doi:10.1080/10717544.2016.1228718
88. Manca ML, Zaru M, Manconi M, et al. Glycosomes: a new tool for effective dermal and transdermal drug delivery. *Int J Pharm.* 2013;455(1–2):66–74. doi:10.1016/j.ijpharm.2013.07.060
89. Essa EA. Effect of formulation and processing variables on the particle size of sorbitan monopalmitate niosomes. *Asia J Pharmaceut.* 2014;4(4). doi:10.22377/ajp.v4i4.289
90. Fouda NH, Abdelrehim RT, Hegazy DA, et al. Sustained ocular delivery of Dorzolamide-HCl via proniosomal gel formulation: in-vitro characterization, statistical optimization, and in-vivo pharmacodynamic evaluation in rabbits. *Drug Deliv.* 2018;25(1):1340–1349. doi:10.1080/10717544.2018.1477861
91. Ali MFM, Salem HF, Abdelmohsen HF, et al. Preparation and clinical evaluation of nano-transfersomes for treatment of erectile dysfunction. *Drug Des Devel Ther.* 2015;9:2431. doi:10.2147/DDDT.S81236
92. Guan P, Lu Y, Qi J, et al. Readily restoring freeze-dried probiosomes as potential nanocarriers for enhancing oral delivery of cyclosporine A. *Colloids Surf B Biointerfaces.* 2016;144:143–151. doi:10.1016/j.colsurf.2016.04.006
93. Ahad A, Raish M, Ahmad A, et al. Eprosartan mesylate loaded bilosomes as potential nano-carriers against diabetic nephropathy in streptozotocin-induced diabetic rats. *Eur J Pharmaceut Sci.* 2018;111:409–417. doi:10.1016/j.ejps.2017.10.012
94. Abdelbary AA, AbouGhaly MH. Design and optimization of topical methotrexate loaded niosomes for enhanced management of psoriasis: application of Box–Behnken design, in-vitro evaluation and in-vivo skin deposition study. *Int J Pharm.* 2015;485(1–2):235–243. doi:10.1016/j.ijpharm.2015.03.020
95. Egawa H, Furusawa K. Liposome adhesion on mica surface studied by atomic force microscopy. *Langmuir.* 1999;15(5):1660–1666. doi:10.1021/la980923w
96. Makino K, Yamada T, Kimura M, et al. Temperature-and ionic strength-induced conformational changes in the lipid head group region of liposomes as suggested by zeta potential data. *Biophys Chem.* 1991;41(2):175–183. doi:10.1016/0301-4622(91)80017-L
97. Abd-Elal RM, Shamma RN, Rashed HM, et al. Trans-nasal zolmitriptan novasomes: in-vitro preparation, optimization and in-vivo evaluation of brain targeting efficiency. *Drug Deliv.* 2016;23(9):3374–3386. doi:10.1080/10717544.2016.1183721
98. Zeisig R, Shimada K, Hirota S, et al. Effect of sterical stabilization on macrophage uptake in vitro and on thickness of the fixed aqueous layer of liposomes made from alkylphosphocholines. *Biochim Biophys Acta.* 1996;1285(2):237–245. doi:10.1016/S0005-2736(96)00167-8
99. Ammar HO, Mohamed MI, Tadros MI, et al. Transdermal delivery of ondansetron hydrochloride via bilosomal systems: in vitro, ex vivo, and in vivo characterization studies. *AAPS PharmSciTech.* 2018;19(5):2276–2287. doi:10.1208/s12249-018-1019-y
100. Ezzat SM, Salama MM, ElMeshad AN, et al. HPLC–DAD–MS/MS profiling of standardized rosemary extract and enhancement of its anti-wrinkle activity by encapsulation in elastic nanovesicles. *Arch Pharm Res.* 2016;39(7):912–925. doi:10.1007/s12272-016-0744-6
101. Singh B, Mehta G, Kumar R, et al. Design, development and optimization of nimesulide-loaded liposomal systems for topical application. *Curr Drug Deliv.* 2005;2(2):143–153. doi:10.2174/1567201053585985
102. Thomas L, Viswanad V. Formulation and optimization of clotrimazole-loaded proniosomal gel using 3<sup>2</sup> factorial design. *Sci Pharm.* 2012;80(3):731–748. doi:10.3797/scipharm.1201-03
103. Singh CH, Jain C, Kumar BN. Formulation, characterization, stability and invitro evaluation of nimesulide niosomes. *Pharmacophore.* 2011;3(3):168–185.
104. Abdelbary GA, Amin MM, Zakaria MY. Ocular ketoconazole-loaded proniosomal gels: formulation, ex vivo corneal permeation and in vivo studies. *Drug Deliv.* 2017;24(1):309–319. doi:10.1080/10717544.2016.1247928
105. Aburahma MH. Bile salts-containing vesicles: promising pharmaceutical carriers for oral delivery of poorly water-soluble drugs and peptide/protein-based therapeutics or vaccines. *Drug Deliv.* 2016;23((6):):1847–1867. doi:10.3109/10717544.2014.976892
106. Mahmood S, Taher M, Mandal UK. Experimental design and optimization of raloxifene hydrochloride loaded nanotransfersomes for transdermal application. *Int J Nanomedicine.* 2014;9:4331. doi:10.2147/IJN.S65408
107. Niu M, Tan YN, Guan P, et al. Enhanced oral absorption of insulin-loaded liposomes containing bile salts: a mechanistic study. *Int J Pharm.* 2014;460(1–2):119–130. doi:10.1016/j.ijpharm.2013.11.028
108. Chieng YY, Chen SB. Interaction and complexation of phospholipid vesicles and triblock copolymers. *J Phys Chem B.* 2009;113(45):14934–14942. doi:10.1021/jp906929u
109. Mohsen AM, Asfour MH, Salama AA. Improved hepatoprotective activity of silymarin via encapsulation in the novel vesicular nanosystem bilosomes. *Drug Dev Ind Pharm.* 2017;43(12):2043–2054. doi:10.1080/03639045.2017.1361968
110. Ammar HO, Ghorab M, El-Nahas SA, et al. Polymeric matrix system for prolonged delivery of tramadol hydrochloride, part I: physicochemical evaluation. *Aaps Pharmscitech.* 2009;10(1):7–20. doi:10.1208/s12249-008-9167-0
111. El Zaafrany GM, Awad GA, Holayel SM, et al. Role of edge activators and surface charge in developing ultra-deformable vesicles with enhanced skin delivery. *Int J Pharm.* 2010;397(1–2):164–172. doi:10.1016/j.ijpharm.2010.06.034

112. Honeywell-Nguyen PL, Bouwstra JA. The in vitro transport of pergolide from surfactant-based elastic vesicles through human skin: a suggested mechanism of action. *J Control Release*. 2003;86(1):145–156. doi:10.1016/S0168-3659(02)00415-7
113. Ahad A, Aqil M, Kohli K, et al. Formulation and optimization of nanotransfersomes using experimental design technique for accentuated transdermal delivery of valsartan. *Nanomedicine*. 2012;8(2):237–249. doi:10.1016/j.nano.2011.06.004
114. Cevc G, Blume G. Hydrocortisone and dexamethasone in very deformable drug carriers have increased biological potency, prolonged effect, and reduced therapeutic dosage. *Biochim Biophys Acta*. 2004;1663(1–2):61–73. doi:10.1016/j.bbame.2004.01.006
115. Mara Mainardes R, Cristina Cocenza Urban M, Oliveira Cinto P, et al. Liposomes and micro/nanoparticles as colloidal carriers for nasal drug delivery. *Curr Drug Deliv*. 2006;3(3):275–285. doi:10.2174/156720106777731019
116. Salama HA, Mahmoud AA, Kamel AO, et al. Brain delivery of olanzapine by intranasal administration of transfersosomal vesicles. *J Liposome Res*. 2012;22(4):336–345. doi:10.3109/08982104.2012.700460
117. Abdelkader H, Longman MR, Alany RG, et al. Phytosome-hyaluronic acid systems for ocular delivery of L-carnosine. *Int J Nanomedicine*. 2016;11:2815. doi:10.2147/IJN.S104774
118. Sabir F, Katona G, Pallagi E, et al. Quality-by-design-based development of n-propyl-gallate-loaded hyaluronic-acid-coated liposomes for intranasal administration. *Molecules*. 2021;26(5):1429. doi:10.3390/molecules26051429
119. Kawar D, Abdelkader H. Hyaluronic acid gel-core liposomes (hyalosomes) enhance skin permeation of ketoprofen. *Pharm Dev Technol*. 2019;24(8):947–953. doi:10.1080/10837450.2019.1572761
120. Tian Z, Liu J, Li N, et al. Hyaluronic acid-coated liposome for active targeting on CD44 expressing tumors. *J Nanoparticle Res*. 2018;20(9):1–10. doi:10.1007/s11051-018-4324-1
121. Pathan AB, Pawar NB, Pathan AJ. Development and optimization of nutraceutical formulation containing citicoline and piracetam. *World J Pharm Res*. 2017;6:586–597 doi:10.20959/wjpr201712-9530.
122. Suzuki H, Ogawa M, Hironaka K, et al. A nifedipine coground mixture with sodium deoxycholate. II. Dissolution characteristics and stability. *Drug Dev Ind Pharm*. 2001;27(9):951–958. doi:10.1081/DDC-100107676
123. Elkomy MH, El-Menshawe SF, Ali AA, et al. Betahistine dihydrochloride transdermal delivery via optimized thermosensitive gels: percutaneous absorption evaluation using rat growth as a biomarker. *Drug Deliv Transl Res*. 2018;8(1):165–177. doi:10.1007/s13346-017-0449-5
124. Al-Amin MM, Chowdury MIA, Saifullah ARM, et al. Levocarnitine improves AIC13-induced spatial working memory impairment in Swiss albino mice. *Front Neurosci*. 2019;13:278. doi:10.3389/fnins.2019.00278
125. Hosseini-Sharifabad A, Rabbani M, Seyed-Yousefi Y, et al. Magnesium increases the protective effect of citicoline on aluminum chloride-induced cognitive impairment. *Clin Psychopharmacol Neurosci*. 2020;18(2):241. doi:10.9758/cpn.2020.18.2.241
126. Wang Z, He C, Shi JS. Natural products for the treatment of neurodegenerative diseases. *Curr Med Chem*. 2020;27(34):5790–5828. doi:10.2174/0929867326666190527120614
127. Abdel-Zaher AO, Hamdy MM, Abdel-Rahman MS, et al. Protective effect of citicoline against aluminum-induced cognitive impairments in rats. *Toxicol Ind Health*. 2017;33(4):308–317. doi:10.1177/0748233716641869
128. Cacabelos R, Carril JC, Cacabelos N, et al. Sirtuins in Alzheimer's disease: SIRT2-related genophenotypes and implications for pharmacogenetics. *Int J Mol Sci*. 2019;20(5):1249. doi:10.3390/ijms20051249
129. Gao J, Zhou R, You X, et al. Salidroside suppresses inflammation in a D-galactose-induced rat model of Alzheimer's disease via SIRT1/NF- $\kappa$ B pathway. *Metab Brain Dis*. 2016;31(4):771–778. doi:10.1007/s11011-016-9813-2
130. Zhang J, Zhao H, Feng Y, et al. Topoisomerase 2 inhibitor etoposide promotes interleukin-10 production in LPS-induced macrophages via upregulating transcription factor Maf and activating PI3K/Akt pathway. *Int Immunopharmacol*. 2021;101:108264. doi:10.1016/j.intimp.2021.108264
131. Simó R, Simó-Servat O, Bogdanov P, et al. Diabetic retinopathy: role of neurodegeneration and therapeutic perspectives. *Asia-Pac J Ophthalmol*. 2021;11(2):160–167. doi:10.1097/APO.0000000000000510
132. Servat O, Russo C, Varela-Sende L, et al. Effects of liposomal formulation of citicoline in experimental diabetes-induced retinal neurodegeneration. *Int J Mol Sci*. 2018;19(8):2458. doi:10.3390/ijms19082458
133. Mohamed NES, Abd El-Moneim AE. Ginkgo biloba extract alleviates oxidative stress and some neurotransmitters changes induced by aluminum chloride in rats. *Nutrition*. 2017;35:93–99. doi:10.1016/j.nut.2016.10.012
134. Saberzadeh J, Arabsolghar R, Takhshid MA. Alpha synuclein protein is involved in Aluminum-induced cell death and oxidative stress in PC12 cells. *Brain Res*. 2016;1635:153–160. doi:10.1016/j.brainres.2016.01.037
135. Henderson LE, Abdelmegeed MA, Yoo SH, et al. Enhanced phosphorylation of Bax and its translocation into mitochondria in the brains of individuals affiliated with Alzheimer's disease. *Open Neurol J*. 2017;11:48. doi:10.2174/1874205X01711010048
136. Frost GR, Li YM. The role of astrocytes in amyloid production and Alzheimer's disease. *Open Biol*. 2017;7(12):170228. doi:10.1098/rsob.170228
137. Simpson DS, Oliver PL. ROS generation in microglia: understanding oxidative stress and inflammation in neurodegenerative disease. *Antioxidants*. 2020;9(8):743. doi:10.3390/antiox9080743
138. Hou L, Sun F, Huang R, et al. Inhibition of NADPH oxidase by apocynin prevents learning and memory deficits in a mouse Parkinson's disease model. *Redox Biol*. 2019;22:101134. doi:10.1016/j.redox.2019.101134
139. Sekino N, Selim M, Shehadah A. Sepsis-associated brain injury: underlying mechanisms and potential therapeutic strategies for acute and long-term cognitive impairments. *J Neuroinflammation*. 2022;19(1):1–14. doi:10.1186/s12974-022-02464-4
140. Bai R, Guo J, Ye XY, et al. Oxidative stress: the core pathogenesis and mechanism of Alzheimer's disease. *Ageing Res Rev*. 2022;77:101619. doi:10.1016/j.arr.2022.101619
141. Butterfield DA, Di Domenico F, Swomley AM, et al. Redox proteomics analysis to decipher the neurobiology of Alzheimer-like neurodegeneration: overlaps in Down's syndrome and Alzheimer's disease brain. *Biochem J*. 2014;463(2):177–189. doi:10.1042/BJ20140772
142. Perluigi M. Redox proteomics analysis to decipher the neurobiology of Alzheimer-like neurodegeneration. *Toxicol Lett*. 2016;258(258):S44. doi:10.1016/j.toxlet.2016.06.1260
143. Cheignon C, Tomas M, Bonnefont-Rousselot D, et al. Oxidative stress and the amyloid beta peptide in Alzheimer's disease. *Redox Biol*. 2018;14:450–464. doi:10.1016/j.redox.2017.10.014

144. Fischer R, Maier O. Interrelation of oxidative stress and inflammation in neurodegenerative disease: role of TNF. *Oxid Med Cell Longev*. 2015;2015:1–18. doi:10.1155/2015/610813
145. Al-Kuraishy HM, Al-Gareeb AI. Citicoline improves human vigilance and visual working memory: the role of neuronal activation and oxidative stress. *Basic Clin Neurosci*. 2020;11(4):423. doi:10.32598/bcn.11.4.1097.1
146. McGlade E, Agoston AM, DiMuzio J, et al. The effect of citicoline supplementation on motor speed and attention in adolescent males. *J Atten Disord*. 2019;23(2):121–134. doi:10.1177/1087054715593633
147. Hosomi S, Ohnishi M, Ogura H, et al. Traumatic brain injury-related inflammatory projection: beyond local inflammatory responses. *Acute Med Surg*. 2020;7(1):e520. doi:10.1002/ams2.520
148. Secades JJ. Citicoline in the treatment of cognitive impairment. *J Neurol Exp Neurosci*. 2019;5(1):14–26. doi:10.17756/jnen.2019-047
149. Siegert S, Seo J, Kwon EJ, et al. The schizophrenia risk gene product miR-137 alters presynaptic plasticity. *Nat Neurosci*. 2015;18(7):1008–1016. doi:10.1038/nn.4023
150. He E, Lozano MAG, Stringer S, et al. MIR137 schizophrenia-associated locus controls synaptic function by regulating synaptogenesis, synapse maturation and synaptic transmission. *Hum Mol Genet*. 2018;27(11):1879–1891. doi:10.1093/hmg/ddy089
151. Siedlecki-Wullich D, Miñano-Molina AJ, Rodríguez-álvarez J. microRNAs as early biomarkers of Alzheimer's disease: a synaptic perspective. *Cells*. 2021;10(1):113. doi:10.3390/cells10010113
152. Guella I, Sequeira A, Rollins B, et al. Evidence of allelic imbalance in the schizophrenia susceptibility gene ZNF804A in human dorsolateral prefrontal cortex. *Schizophr Res*. 2014;152(1):111–116. doi:10.1016/j.schres.2013.11.021
153. Kos A, Aschrafi A, Nadif Kasri N. The multifarious hippocampal functions of microRNA-137. *Neuroscientist*. 2016;22(5):440–446. doi:10.1177/1073858415608356
154. Bielefeld P, Schouten M, Meijer GM, et al. Co-administration of anti microRNA-124 and-137 oligonucleotides prevents hippocampal neural stem cell loss upon non-convulsive seizures. *Front Mol Neurosci*. 2019;12:31. doi:10.3389/fnmol.2019.00031
155. Kim B, Tag SH, Kim YS, et al. Circulating microRNA miR-137 as a stable biomarker for methamphetamine abstinence. *Psychopharmacology*. 2022;239(3):831–840. doi:10.1007/s00213-022-06074-z
156. Mahmoudi E, Cairns MJ. MiR-137: an important player in neural development and neoplastic transformation. *Mol Psychiatry*. 2017;22(1):44–55. doi:10.1038/mp.2016.150
157. Li Y, Jin L, Wang F, et al. Epigenetic axis of SNHG19/miR-137/TNFAIP1 modulates amyloid beta peptide 25–35-induced SH-SY5Y cytotoxicity. *Epigenomics*. 2022;14(4):187–198. doi:10.2217/epi-2021-0288
158. Xu P, Wang Y, Deng Z, et al. MicroRNA-15a promotes prostate cancer cell ferroptosis by inhibiting GPX4 expression. *Oncol Lett*. 2022;23(2):1–8. doi:10.3892/ol.2022.13186
159. Shekari N, Asadi M, Akbari M, et al. Autophagy-regulating microRNAs: two-sided coin in the therapies of breast cancer. *Eur Rev Med Pharmacol Sci*. 2022;26(4):1268–1282. doi:10.26355/eurrev\_202202\_28120
160. Almuhayawi MS, Ramadan WS, Harakeh S, et al. The potential role of pomegranate and its nano-formulations on cerebral neurons in aluminum chloride induced Alzheimer rat model. *Saudi J Biol Sci*. 2020;27(7):1710–1716. doi:10.1016/j.sjbs.2020.04.045
161. Abdel-Salam O, Youness ER, Mohammed NA, et al. Citicoline protects against tramadol-induced oxidative stress and organ damage. *Reactive Oxygen Species*. 2019;7(20):106–120 doi:10.20455/ros.2019.823.
162. Bekhet MA, Ali AA, Kharshoum RM, et al. Intranasal niosomal in situ gel as a novel strategy for improving citicoline efficacy and brain delivery in treatment of epilepsy: in vitro and ex vivo characterization and in vivo pharmacodynamics investigation. *J Pharm Sci*. 2022;111(8):2258–2269. doi:10.1016/j.xphs.2022.02.012
163. Messiha BA, Ali MR, Khattab MM, et al. Perindopril ameliorates experimental Alzheimer's disease progression: role of amyloid  $\beta$  degradation, central estrogen receptor and hyperlipidemic-lipid raft signaling. *Inflammopharmacology*. 2020;28(5):1343–1364. doi:10.1007/s10787-020-00724-4
164. Liu W, Li J, Yang M, et al. Chemical genetic activation of the cholinergic basal forebrain hippocampal circuit rescues memory loss in Alzheimer's disease. *Alzheimers Res Ther*. 2022;14(1):1–20 doi:10.1186/s13195-022-00994-w.
165. Séguy L, Groo AC, Malzert-Fréon A. How nano-engineered delivery systems can help marketed and repurposed drugs in Alzheimer's disease treatment?. *Drug Discov Today*. 2022;27(6):1575–1589. doi:10.1016/j.drudis.2022.02.022
166. Skopiński P, Radomska-Leśniewska DM, Izdebska J, et al. New perspectives of immunomodulation and neuroprotection in glaucoma. *Cent Eur J Immunol*. 2021;46(1):105–110. doi:10.5114/ceji.2021.104329

International Journal of Nanomedicine

Dovepress

Publish your work in this journal

The International Journal of Nanomedicine is an international, peer-reviewed journal focusing on the application of nanotechnology in diagnostics, therapeutics, and drug delivery systems throughout the biomedical field. This journal is indexed on PubMed Central, MedLine, CAS, SciSearch®, Current Contents®/Clinical Medicine, Journal Citation Reports/Science Edition, EMBASE, Scopus and the Elsevier Bibliographic databases. The manuscript management system is completely online and includes a very quick and fair peer-review system, which is all easy to use. Visit <http://www.dovepress.com/testimonials.php> to read real quotes from published authors.

Submit your manuscript here: <https://www.dovepress.com/international-journal-of-nanomedicine-journal>